MUSE-ALMA haloes VI: coupling atomic, ionized, and molecular gas kinematics of galaxies

Roland Szakacs, Céline Péroux, Martin Zwaan, Aleksandra Hamanowicz, Anne Klitsch, Alejandra Fresco, Ramona Augustin, Andrew Biggs, Varsha Kulkarni, Hadi Rahmani

Monthly Notices of the ROYAL ASTRONOMICAL SOCIETY

MNRAS **505,** 4746–4761 (2021) https://doi.org/10.1093/mnras/stab1434
Advance Access publication 2021 June 5

MUSE-ALMA haloes VI: coupling atomic, ionized, and molecular gas kinematics of galaxies

Roland Szakacs,[1]★ Céline Péroux,[1,2] Martin Zwaan,[1] Aleksandra Hamanowicz,[3] Anne Klitsch,[4] Alejandra Y. Fresco,[5] Ramona Augustin,[3] Andrew Biggs,[1] Varsha Kulkarni[6] and Hadi Rahmani[2,7]

[1]*European Southern Observatory (ESO), Karl-Schwarzschild-Str. 2, D-85748 Garching bei München, Germany*
[2]*Aix Marseille Univ, CNRS, CNES, LAM, F-13013 Marseille, France*
[3]*Space Telescope Science Institute, 3700 San Martin Dr, Baltimore, MD 21218, USA*
[4]*DARK, Niels Bohr Institute, University of Copenhagen, Jagtvej 128, DK-2200 Copenhagen, Denmark*
[5]*Max-Planck-Institut für Extraterrestrische Physik (MPE), Giessenbachstr. 1, D-85748 Garching bei München, Germany*
[6]*University of South Carolina, Department of Physics and Astronomy, 712 Main Street, Columbia, SC 29208, USA*
[7]*GEPI, Observatoire de Paris, PSL Université, CNRS, 5 Place Jules Janssen, F-92190 Meudon, France*

Accepted 2021 May 10. Received 2021 April 27; in original form 2020 December 4

ABSTRACT

We present results of MUSE-ALMA haloes, an ongoing study of the circumgalactic medium (CGM) of galaxies ($z \leq 1.4$). Using multiphase observations we probe the neutral, ionized, and molecular gas in a subsample containing six absorbers and nine associated galaxies in the redshift range $z \sim 0.3$–0.75. Here, we give an in-depth analysis of the newly CO-detected galaxy Q2131−G1 ($z = 0.42974$), while providing stringent mass and depletion time limits for the non-detected galaxies. Q2131−G1 is associated with an absorber with column densities of $\log(N_{\rm H\,I}/{\rm cm}^{-2}) \sim 19.5$ and $\log(N_{\rm H_2}/{\rm cm}^{-2}) \sim 16.5$, and has a star formation rate of SFR $= 2.00 \pm 0.20\,{\rm M}_\odot{\rm yr}^{-1}$, a dark matter fraction of $f_{\rm DM}(r_{1/2}) = 0.24$–$0.54$, and a molecular gas mass of $M_{\rm mol} = 3.52^{+3.95}_{-0.31} \times 10^9\ {\rm M}_\odot$ resulting in a depletion time of $\tau_{\rm dep} < 4.15$ Gyr. Kinematic modelling of both the CO (3–2) and [O III] λ5008 emission lines of Q2131−G1 shows that the molecular and ionized gas phases are well aligned directionally and that the maximum rotation velocities closely match. These two gas phases within the disc are strongly coupled. The metallicity, kinematics, and orientation of the atomic and molecular gas traced by a two-component absorption feature are consistent with being part of the extended rotating disc with a well-separated additional component associated with infalling gas. Compared to emission-selected samples, we find that H I-selected galaxies have high molecular gas masses given their low star formation rate. We consequently derive high depletion times for these objects.

Key words: galaxies: disc – galaxies: haloes – galaxies: ISM – galaxies: kinematics and dynamics – quasars: absorption lines – dark matter.

1 INTRODUCTION

One of the most puzzling questions in galaxy evolution is how galaxies sustain their star formation. Due to the short depletion time-scales that have been observed, it is evident that galaxies have to accrete gas from an external source in order to maintain their continuity on the main sequence (e.g. Scoville et al. 2017). The inflowing gas is accreted from the intergalactic medium (IGM). While it is a challenging task to observe the accretion process due to the low density of the extragalactic gas, a number of inflows have been observed over the last few years (e.g. Martin et al. 2012; Rubin et al. 2012; Turner et al. 2017; Zabl et al. 2019). Metal enriched gas is also expelled from galaxies due to active galactic nucleus (AGN) feedback (Shull, Danforth & Tilton 2014) or stellar feedback (e.g. Ginolfi et al. 2020). A fraction of the expelled gas is returned through galactic fountains (Fraternali 2017; Bish et al. 2019), where cooled down gas rains on to the galactic disc, while some other part is returned to the IGM through galactic winds driven by AGN and stellar feedback processes.

The inflowing and outflowing gas interacts in a zone called the circumgalactic medium (CGM), which is loosely defined as the gas surrounding galaxies outside of the disc or interstellar medium, but within the virial radius (Tumlinson, Peeples & Werk 2017). While it can be a challenging endeavour to observe the CGM directly, due to the low surface brightness of the gas (e.g. Frank et al. 2012; Augustin et al. 2019; Corlies et al. 2020), observations and simulations indicate that the CGM is a multiphase medium. The hot phase of the CGM has been observed through X-ray observations (e.g. Anderson & Bregman 2010; Anderson, Bregman & Dai 2013; Bregman et al. 2018; Nicastro et al. 2018) and Ly α emission (e.g. Cantalupo et al. 2014; Wisotzki et al. 2016, 2018; Umehata et al. 2019). The cooler gas in the CGM can be probed by studying absorption lines in quasar (QSO) spectra, which offer the advantage of the sensitivity being independent of redshift (e.g. Tripp, Lu & Savage 1998). This cooler low density gas has been detected through the absorption lines of various metal species and Hydrogen (e.g. Steidel et al. 2010; Rudie et al. 2012; Werk et al. 2013; Turner et al. 2014). Hydrodynamic

★ E-mail: roland.szakacs@eso.org

simulations strengthen the picture of a multiphase CGM, by finding a mixture of cooler ($T \sim 10^4$ K) and hotter ($T \sim 10^{5.5}$–10^6 K) gas within the virial radius of simulated galaxies (e.g. Stinson et al. 2012; Suresh et al. 2017; Nelson et al. 2020).

An important aspect to understand how galaxies sustain their star formation is to connect the CGM gas probed by absorption with the galaxies associated with the absorbers. Narrow-band imaging and long-slit spectroscopic studies have searched for nebular emissions from H I-selected galaxies (e.g. Kulkarni et al. 2000, 2001) and have, in part, been successful in the past (e.g. Chen, Kennicutt & Rauch 2005; Fynbo et al. 2010). Further, integral field spectroscopy (IFS) combined with long-slit spectroscopy follow-ups have made it possible to not only associate galaxies with strong H I absorbers (e.g. Bouché et al. 2007; Péroux et al. 2011a,b, 2017; Rudie, Newman & Murphy 2017), but to also study the star formation rate (SFR), metallicity of the emission line gas, and kinematics of the ionized gas (e.g. Bouché et al. 2012; Péroux et al. 2017; Rahmani et al. 2018a,b; Hamanowicz et al. 2020). The findings, among others, include a correlation between the SFR of the associated galaxy and the equivalent width of the absorption, indicating a physical connection between star bursts and gas seen in absorption (Bouché et al. 2007). Péroux et al. (2011a) find that in the majority of the cases the metallicity of the absorption is lower than of the associated galaxy. The number of studies associating absorption features found in the spectra of quasars with physical properties of absorber host candidates is low. An additional issue remains: associating galaxies with absorbers that are in complex group environments as studied in this and a previous MUSE-ALMA haloes publication (Hamanowicz et al. 2020). The authors suggest that galaxies found in these environments would benefit from associating the kinematics of the galaxies with the absorber in order to distinguish which galaxies/environments the absorption is tracing (e.g. see Rahmani et al. 2018a). Therefore obtaining more observations of absorber–absorber host systems plays a key part in furthering the understanding of the medium surrounding galaxies.

Searches at the radio/sub-mm wavelengths with instruments like the Atacama Large Millimeter Array (ALMA) have enabled the community to study the mass, depletion time, and kinematics of the molecular gas in galaxies associated with absorbers (e.g. Neeleman et al. 2016, 2018; Møller et al. 2017; Augustin et al. 2018; Kanekar et al. 2018, 2020; Klitsch et al. 2018, 2019b; Péroux et al. 2019; Freundlich et al. 2021). One of the findings that these H I-selected galaxies have in common is that the molecular gas masses of these galaxies are high for their given SFR, leading to depletion times that are up to multiple factors larger than the averages found in emission selected galaxies. Further observations and constructing statistically significant samples, like the ones obtained in the MUSE-ALMA haloes project, are needed in order to study a possible correlation.

Obtaining spatially resolved multiphase data of galaxies have furthered our understanding in how the ionized and molecular gas phases relate to each other. Kinematic studies have revealed that the two phases mostly align well spatially (e.g. Møller et al. 2017; Klitsch et al. 2018; Übler et al. 2018; Loiacono et al. 2019; Molina et al. 2019, 2020; Péroux et al. 2019). Further kinematic studies by the EDGE-CALIFA survey (Levy et al. 2018) have shown that 75 per cent of the galaxies in their sample have higher maximum rotational velocities for the molecular gas while the remaining 25 per cent have similar maximum rotational velocities to the ionized gas. Péroux et al. (2019) on the other hand did indeed find a case where the rotational velocity of the molecular gas was significantly lower than for the ionized gas in a galaxy associated with a strong H I absorber. The number of galaxies observed in both the molecular and ionized gas phase is still low and studies of these gas phases is a key point in furthering our understanding of gas flows within and surrounding galaxies.

Another aspect of using IFS-based multiwavelength observations is that these data make it possible to estimate the dark matter fractions in the inner parts of galaxies. A widely accepted notion is that dark matter dominates the outskirts of galaxies, however the distribution of matter in the central parts of galaxies is still debated. Studies like the DiskMass survey (Martinsson et al. 2013) have observed 30 spiral galaxies at the current epoch and found the central dark matter fractions to be mostly in the range of 0.5–0.9. Studies of higher redshift galaxies find lower central dark matter fractions in both observations and simulations (e.g. Übler et al. 2018, 2021; Genzel et al. 2017, 2020). Price et al. (2020) report a decrease of the dark matter fraction toward higher redshifts, attributed to various intertwined effects of galaxy mass-size growth, gas fraction, and halo growth and evolution. Therefore obtaining further samples of central dark matter fractions are an important aspect of understanding the reasons for the differences in the central dark matter fractions over different epochs.

The studied MUSE-ALMA haloes subsample includes six absorbers and nine associated galaxies in the redshift range $z \sim 0.3$–0.75. In this publication, we present the results from new ALMA observations of the fields Q2131−1207, Q1232−0224, Q0152−2001, Q1211−1030, and Q1130−1449 each of which contains a strong H I absorber at $z \sim 0.4$ and in the case of Q1232−0224 an additional one at $z \sim 0.75$. While we analyse and provide information on all fields, the focus of this publication lies on the CO-detected galaxy Q2131−G1 in the field Q2131−1207 [first reported in Bergeron (1986) and further analysed in Guillemin & Bergeron (1997) and Kacprzak et al. (2015)].

The paper is organized as follows: Section 2 presents the observational set-up and data reduction and imaging process. Section 3 describes the molecular properties of the galaxies associated with the strong H I absorbers, while describing both the physical and morpho-kinematical properties and providing limits for non-detections. In Section 4, we discuss our findings and put them into context with previous observations. Finally, Section 5 gives a summary of the findings. Throughout this paper we adopt an $H_0 = 70\,\mathrm{km\,s^{-1}\,Mpc^{-1}}$, $\Omega_\mathrm{M} = 0.3$, and $\Omega_\Lambda = 0.7$ cosmology.

2 OBSERVATIONS

We follow a multiwavelength approach in order to study the gas and associated galaxies in this study, combining VLT/MUSE, *HST*, and ALMA observations. The observations and corresponding data processing/imaging are presented in this section.

2.1 Optical campaign

2.1.1 VLT/MUSE observations

In this work, we study five fields containing quasar absorbers (Q2131−1207, Q1232−0224, Q0152−2001, Q1211+1030, and Q1130−1449). These fields are a subset of the full MUSE-ALMA haloes sample which have ALMA follow-up observations targeting redshifts of $z \sim 0.4$ and $z \sim 0.75$. That sample has been observed using VLT/MUSE in period 96 under programme ESO 96.A-0303 (PI: C. Peroux). All fields were observed in nominal mode (4800–9400 Å) under good seeing conditions (<0.85 arcsec). The first four fields were observed for 1–2 h per target, while Q1130−1449 was observed significantly deeper (12×1200 s). The observations and data reduction method for the five quasar fields is described

in depth in Péroux et al. (2019) and Hamanowicz et al. (2020). In short, the ESO MUSE reduction pipeline v2.2 (Weilbacher, Streicher & Palsa 2016) was used. Bias, flat and wavelength calibration was applied in addition to line spread functions and illumination correction frames to each individual exposure. These astrometry solutions and the correction for geometry and flux calibrations where then applied. Each of the individual exposures was combined including field rotation. Instead of the pipeline sky subtraction method, the sky emission lines were removed using a principal component analysis algorithm (Husemann et al. 2016). Additionally, the MUSE observations for the fields have been discussed in depth in the following publications: Q0152−020 (Rahmani et al. 2018a; Rahmani et al. 2018b; Hamanowicz et al. 2020); Q1130−1449 (Péroux et al. 2019; Hamanowicz et al. 2020); Q2131−1207 (Péroux et al. 2017; Hamanowicz et al. 2020); Q1232−0224, Q1211−1030 (Hamanowicz et al. 2020).

2.1.2 HST *observations*

We select fields that show strong H I absorption column densities in quasar spectra. The column densities are based on literature and were derived using data from the Faint Object Spectrograph (FOS) and Cosmic Origins Spectrograph (COS) on *HST* [see Boissé et al. (1998) for details about the Q2131z039$_{\rm H\,I}$ absorber; Lane et al. (1998) for Q1130z031$_{\rm H\,I}$; Rao, Turnshek & Nestor (2006) for Q1232z075$_{\rm Mg\,II}$; Muzahid et al. (2016) for Q2131z043$_{\rm H\,I}$ and 1211z039$_{\rm H\,I}$; Rahmani et al. (2018b) for Q0152z038$_{\rm H\,I}$].

Readily available and reduced archival *HST* imaging is used for observations of the stellar continuum. The exposure times for the five fields range from 10 to 50 min. Observations of Q2131−1207 (PI: Maccheto, ID:5143), Q1232−0224 (PI: Bergeron, ID:5351), Q0152−2001 (PI: Steidel, ID:6557), and Q1211+1030 (PI: Bergeron, ID:5351) use the Wide Field Planetary Camera 2 (WPFC2) in the F702W filter. The observation of Q1130−1449 (PI: Bielby, ID: 14594) uses the Wide Field Camera 3 (WFC3) in filter IR-F140W.

Further archival *HST* data, obtained with the COS on *HST*, are used for studying the H_2 absorption lines of the absorber associated with Q2131−G1. Specifically, we use these spectra to study the position of the H_2 absorption line in velocity space. The H_2 absorption has been extensively studied in Muzahid et al. (2016). We use two observations with a wavelength range of 1140–1800Å , which consist of G130M (exposure time: 77 min) and G160M (exposure time: 120 min) FUV grating integrations at a medium resolution of $R \sim 20\,000$ (corresponding to a full width at half-maximum (FWHM) of ~ 18 km s^{-1}; PI: Churchill, ID: 13398). Due to the Lyman-limit break of the absorber ($z = 0.43$) there is no recorded QSO flux at wavelengths below 1310 Å.

Additionally, we have an ongoing *HST* multiband photometry program of 40 orbits (PI: Péroux, ID: 15939). This program will allow us to study the morphology and stellar masses of galaxies associated with H I absorbers in the MUSE-ALMA haloes survey.

This program will allow us to study the morphology and stellar masses of 200 $z < 1.2$ galaxies associated with H I and Mg II absorbers (including our current sample) in more detail at a later stage of the MUSE-ALMA haloes project.

2.2 ALMA observations

2.2.1 *Observation details*

The fields Q2131−1207, Q1232−0224, Q0152−2001, and Q1211+1030 were observed with ALMA in Band 6 in order to cover the CO(3–2) lines of galaxies associated with absorbers found at $z \sim 0.4$ (programme 2017.1.00571.S, PI: C. Peroux). Given the field of view (FOV) of ALMA in band 6 we target a subset of galaxies previously observed with MUSE with impact parameters ranging from 8 to 82 kpc. All of the fields have one spectral window that was centred on the redshifted CO(3–2) frequency of 345.796 GHz with a high spectral resolution mode. This results in 3840 channels, each with a 1.129 MHz width. Additional three other spectral windows are also included for these observations in a low spectral resolution mode (31.250 MHz). The CO(3–2) line of one the galaxies in the field Q1232−0224 ($z = 0.7566$) is expected to be in one of the low-resolution spectral windows. We also include the previously studied field Q1130−1449 in our analysis. Details concerning this observation can be found in Péroux et al. (2019).

A table with the quasar coordinates, observation dates, exposure times, angular resolution, used calibrators, percipitable water vapour (PWV), and antenna configurations for the different observed fields can be found in Table A1 in Appendix A.

2.2.2 *Data reduction and imaging*

In this section, we describe the image processing of the fields Q2131−1207, Q1232−0224, Q0152−2001, and Q1211−1449 observed with ALMA. The fields are imaged and, when possible, self-calibrated using the Common Astronomy Software Applications package (CASA; McMullin et al. 2007) version 5.6.2–3.

As a starting point for all imaging and calibration the pipeline-calibrated *uv* data sets as delivered by ALMA-ARC are used. When multiple measurement sets are provided due to multiple observations, we combine them using the `concat` task. Using these combined measurement sets we reconstruct an initial continuum image of the field by using the task `tclean`. Depending on the synthesized beam size, we use different pixel sizes for the imaging (0.18 arcsec for Q0152−2001, 0.17 arcsec for Q1211−1030, 0.2 arcsec for Q2131−G1, and 0.22 arcsec for Q1232−0224). For all data sets we use `tclean` with a Briggs weighting scheme with the robust parameter set to 1.0, a standard gridder and a hogbom deconvolver.

In the case of Q0152−2001 and Q1211−1030 we follow up `tclean` with the task `uvcontsub` in order to subtract the central quasar in the field. As a final step we use the continuum-subtracted *uv* data set and the task `tclean` with the same parameters as for the continuum images and a spectral binning of 50 km s^{-1}.

Both the quasars in Q2131−1207 and Q1232−0224 are bright at mm-wavelengths, allowing us to perform self-calibration. Therefore, after creating the initial model and continuum image mentioned above, we calculate the temporal gains using the task `gaincal` with gaintype `G` (which determines the gains for each polarization and spectral window) using a solution interval of 35 s for Q2131−1207 and 70 s for Q1232−0224. For both calibrations we check that the solutions show a smooth evolution over time and that the solutions have an acceptable signal-to-noise ratio (SNR) > 10. Then we apply the solutions to the measurement sets using the task `applycal` in linear interpolation mode and create an updated sky model and continuum image using `tclean`. Following the phase calibration we proceeded with a second round of amplitude calibration using gaintype G and a solution interval of 105 s for Q2131−1207 and 70 s for Q1232−0224. Following this we create another updated sky model and continuum image using `tclean`. Then we follow up with the continuum subtraction using `uvcontsub` with order 3 for Q2131−1207 and 2 for Q1232−0224. We use the continuum-subtracted data set to create a data cube using `tclean` with the

same parameters as for the continuum images and a spectral binning of 50 km s^{-1}. As the final step we produce a cube corrected for the primary beam using the `impbcor` task. The final RMS for the cubes where self-calibration was feasible is $\sim 1.5 \times 10^{-4}$ Jy. The cubes where no self-calibration was possible have an RMS $\sim 2.8 \times 10^{-4}$ Jy.

3 MOLECULAR GAS PROPERTIES OF THE GALAXIES ASSOCIATED WITH THE ABSORBERS

We target nine galaxies in the redshift range $z = 0.31$–0.76. Out of those nine galaxies we detect four: the previously detected galaxies Q1130−G2, Q1130−G4, and Q1130−G6 (presented in Péroux et al. 2019) and the newly CO-detected galaxy Q2131−G1. We provide an analysis of the physical and morpho-kinematical properties of Q2131−G1 in this section. Additionally, we provide stringent limits on the molecular gas content of undetected galaxies. All the calculated physical properties of the targeted galaxies can be found in Table 1 and the morpho-kinematical properties are listed in Table 2.

3.1 Properties of the CO-detected galaxy (Q2131−G1, $z = 0.42974$)

In this section we describe the physical and morpho-kinematical properties of the CO-detected galaxy Q2131−G1 and the galaxy–gas (absorber) connection.

3.1.1 Molecular gas mass and depletion time

We study the molecular gas properties of the CO-detected galaxy Q2131−G1. We create an integrated flux map using the CASA task `immoments` and set the threshold of pixels to be counted above $\sim 2\sigma$ of the created cube. This integrated flux map yields an observed CO(3–2) flux of $S_{\rm CO} = (0.36 \pm 0.02)$ Jy km s^{-1}. We derive the CO(1-0) luminosity by first calculating $L'_{\rm CO(3-2)}$ using $S_{\rm CO}$ and the prescription by Solomon, Downes & Radford (1992). Then we use the $L'_{\rm CO(3-2)}$ to $L'_{\rm CO(1-0)}$ conversion factor from Fixsen, Bennett & Mather (1999): $L'_{\rm CO(3-2)}/L'_{\rm CO(1-0)} = 0.27$ and obtain a CO(1-0) luminosity of $L'_{\rm CO(1-0)} = (1.42 \pm 0.08) \times 10^9$ K km s^{-1} pc^2. We choose the Milky Way spectral line energy distribution conversion factor due to the rather low redshift of the galaxy ($z = 0.42974$). We note that absorption-selected systems may preferentially select interacting galaxies, which have more excited CO SLEDs than isolated galaxies making the used SLED a first order approximation for Q2131−G1 (Klitsch et al. 2019a). The molecular mass is calculated by using the geometric mean of the Bolatto, Wolfire & Leroy (2013) and Genzel et al. (2012) $\alpha_{\rm CO}$(Z) prescription. This conversion factor is a good approximation for galaxies which are not significantly below solar metallicity and therefore appropriate for Q2131−G1 (12+log(O/H) $= 8.98 \pm 0.02$ (Péroux et al. 2017), also see Genzel et al. (2015) for a more detailed description of this averaged conversion factor). We note that Muzahid et al. (2016) derived a lower metallicity, closer to the solar metallicity, for Q2131−G1 (12+log(O/H) $= 8.68 \pm 0.09$). This discrepancy can be explained by the use of the N2-index, which is known to saturate at solar metallicities (Pettini & Pagel 2004). We elect to use the R_{23} based metallicity by Péroux et al. (2017), but note that the metallicity is based on emission line fluxes that have not been dust-corrected and therefore possibly overestimate the metallicity. We therefore base the conversion factor on 12+log(O/H) $= 8.98 \pm 0.02$, but include the lower metallicity in the error calculation and compute $\alpha_{\rm CO} = 2.48^{+2.50}_{-0.08}$ M$_\odot$(K km/s pc)$^{-1}$. The molecular mass is $M_{\rm mol} = 3.52^{+3.95}_{-0.31} \times 10^9M_\odot$. The calculated molecular mass is consistent with the mass limit of $M_{\rm mol} \leq 8.2 \times 10^9M_\odot$ using $L'_{\rm CO(2-1)} \leq 3.8 \times 10^9$K km s^{-1}pc^2 (Klitsch et al. 2021).

Using the non-dust corrected SFR derived by Hamanowicz et al. (2020; SFR$_{\rm [O\,II]} = 2.00 \pm 0.2$ M$_\odot$ yr^{-1}), we calculate the limit on the depletion time using

$$\tau_{\rm dep} < \frac{M_{\rm mol,max}}{\rm SFR_{[O\,II,min]}} \rm yr. \quad (1)$$

The depletion time for Q2131−G1 is $\tau_{\rm dep} < 4.15$ Gyr.

3.1.2 Stellar mass

In this section we estimate the stellar mass of Q2131−G1. The stellar mass is derived from the mass–metallicty–relation (MZR) (Tremonti et al. 2004). This relation is based on ∼53 000 galaxies at $z \sim 0.1$ from the Sloan Digital Sky Survey (SDSS) sample and holds for $8.5 < \log(M_\star/{\rm M}_\odot) < 11.5$. Using the metallicity derived by Péroux et al. (2017; 12+log(O/H) $= 8.98 \pm 0.02$), we get two solutions: $\log(M_\star/{\rm M}_\odot) = 10.1 \pm 0.1$ and $\log(M_\star/{\rm M}_\odot) = 12.9 \pm 0.1$. This relation does not hold for the second solution, as that stellar mass would be outside of the valid range. We attempt to break this degeneracy by applying the Tully–Fisher relation (linking the stellar mass with the maximum rotation velocity of the galaxy; Tully & Fisher 1977). We used the relation by Puech et al. (2008), derived from a sample of $z \sim 0.6$ galaxies using kinematics from the [O II] line. Using $V_{\rm max} = 200 \pm 3$ km s^{-1} [as derived by the kinematical analysis of the [O III] λ5008 line in Péroux et al. (2017)], we estimate the stellar mass of G2131−G1 to be $\log(M_\star/{\rm M}_\odot) = 10.54 \pm 0.71$. This stellar mass is consistent with the lower stellar mass derived from the MZR. For further calculations we decide to use the stellar mass derived from the MZR, but take into account the value derived by the Tully–Fisher relation and by the MZR using the Muzahid et al. (2016) metallicity (12+log(O/H) $= 8.68 \pm 0.09$, $\log(M_\star/{\rm M}_\odot) = 9.1^{+0.3}_{-0.2}$) in the error calculations: $\log(M_\star/{\rm M}_\odot) = 10.1^{+0.5}_{-1.0}$

3.1.3 Dark matter fraction

Current studies have shown a declining dark matter fraction with increasing redshift (e.g. Genzel et al. 2020; Price et al. 2020). We constrain the dark matter contribution to the galaxy within the half-light radius. We create an NFW-profile (Navarro, Frenk & White 1997) based on the halo mass estimate (see Section 3.1.1) and compute the corresponding cumulative mass curve. We note that this is a first-order approximation of the dark matter fraction within the central region of G2131−G1.

The halo mass estimate is based on abundance matching (e.g. Behroozi, Conroy & Wechsler 2010; Moster et al. 2010; Moster, Naab & White 2018). We use the prescription provided in Genzel et al. (2020, their equation A13, provided in a private communication with B. Moster) based on the galaxy–halo pairs from Moster et al. (2018) to fit a halo mass–galaxy mass relation. This relation is appropriate for $z > 0.5$ and provides an estimate of the halo mass derived from the stellar mass. Using the stellar mass of $\log(M_\star/{\rm M}_\odot) = 10.1^{+0.5}_{-1.0}$, we compute a halo mass of $\log(M_{200}/{\rm M}_\odot) = 11.6 \pm 0.5$. This halo mass is consistent with the halo mass derived by Péroux et al. (2017) assuming a spherical virialized collapse model by Mo & White (2002; $\log(M_{200}/{\rm M}_\odot) = 12.46^{+0.03}_{-0.04}$). The corresponding radius (r_{200}), within which the mean mass density is

Table 1. Physical properties of absorption-selected galaxies. Row 1 – absorber: (1) reference name of the absorber used in this paper, (2) redshift of the absorber, (3) H I column density of the absorber, and (4) metallicity of the absorber. Row 2 – galaxy: (1) reference name of the galaxy used in this paper and its redshift in brackets, (2) impact parameter in kpc and arcseconds, (3) star formation rate measured from the [O II] emission line (not dust corrected), (4/5) lower/upper metallicity 12+log(O/H) (not dust corrected, both metallicity branches derived by Hamanowicz et al. (2020) are displayed following Kobulnicky, Kennicutt & Pizagno 1999). If only one metallicity branch is reported in literature, the upper column is left blank. (6) Observed CO flux density, (7) CO velocity width, (8) CO(1-0) luminosity, (9) molecular mass, and (10) depletion time-scale of the galaxy. Literature references: [a]Hamanowicz et al. (2020), [b]Muzahid et al. (2016), [c]Boissé et al. (1998), [d]Rao et al. (2006), [e]Rahmani et al. (2018b), [f]Lane et al. (1998), and [g]Péroux et al. (2019).

Absorber ID Galaxy | (z)	z_{abs} [a] b [a] [kpc arcsec^{-1}]	$\log(N_{HI,\,abs})$ (cm^{-2}) $SFR_{[O\,II]}$ [a] ($M_\odot$ yr^{-1})	$[Fe/H]_{abs}$ $12+\log(O/H)_l$ [a]	$12+\log(O/H)_u$ [a]	f_{CO} (GHz)	S_{CO} (Jy km s^{-1})	$FWHM_{CO}$ (km s^{-1})	$L_{CO(1-0)}$ (10^9 K km s^{-1}pc^2)	M_{mol} (10^9 $M_\odot$)	τ_{dep} (Gyr)
Q2131z043$_{HI}$	**0.43**	**19.5 ± 0.15** [b]	**> −0.96** [a]							
Q2131−G1 | (0.42974)	52 / 9.2	2.00 ± 0.2	8.98 ± 0.02	–	241.866	0.36 ± 0.02	184 ± 50	1.42 ± 0.08	$3.52^{+3.95}_{-0.31}$	< 4.15
Q2131−G2 | (0.4307 [a])	61 / 10.7	0.20 ± 0.1	8.32 ± 0.16	–	241.697	< 0.068	–	< 0.27	< 3.64	< 36.37
Q1232z039$_{HI}$	**0.3950**	**20.75 ± 0.07** [c]	**< −1.31** [c]							
Q1232−G1 | (0.3953 [a])	8 / 1.5	0.67 ± 0.09	8.02 ± 0.06	8.66 ± 0.04	247.829	< 0.070	–	< 0.24	< 6.09	< 8.02
Q1232z075$_{Mg\,II}$	**0.7572**	**$18.36^{+0.09}_{-0.08}$** [d]	**> −1.48** [d]							
Q1232−G2 | (0.7566[a])	68 / 9.1	2.58 ± 0.23	8.19 ± 0.19	8.54 ± 0.19	262.462	< 0.12	–	< 0.83	< 18.31	< 7.80
Q0152z038$_{HI}$	**0.3887**	**<18.8** [e]	**> −1.36** [a]							
Q0152−G1 | (0.3826[a])	60 / 11.5	1.04 ± 0.03	8.65 ± 0.09	–	250.105	< 0.17	–	< 0.53	< 2.80	< 2.78
Q1211z039$_{HI}$	**0.3929**	**19.46 ± 0.08** [b]	**> −1.05** [a]							
Q1211−G1 | (0.3928 [a])	37 / 6.8	4.71 ± 0.08	8.16 ± 0.01	8.48 ± 0.01	248.274	< 0.15	–	< 0.49	< 6.78	< 1.47
Q1130z031$_{HI}$	**0.3127**	**21.71 ± 0.07** [f]	**−1.94 ± 0.08** [g][1]							
Q1130−G2 | (0.3127 [a])	44 / 9.5	0.44 ± 0.3	8.77 ± 0.05	–	263.4	0.63 ± 0.01 [g]	250 ± 50 [g]	3.1 ± 0.1[g]	$11.03^{+1.44}_{-1.27}$	25^{+21}_{-20}
Q1130−G4 | (0.3126)	82 / 17.7	>0.40	<8.65	–	263.44	0.42 ± 0.03[g]	535 ± 50 [g]	2.1 ± 0.1[g]	> 8.88	⩾22.19
Q1130−G6 | (0.3115[a])	98 / 21.3	1.14 ± 0.7	8.94 ± 0.16	–	263.67	0.20 ± 0.01[g]	205 ± 50 [g]	1.0 ± 0.1[g]	$2.65^{+1.20}_{-0.82}$	$2.3^{+1.4}_{-1.1}$

Note. [1]We note that Kanekar et al. (2009) report a higher metallicity of $[Z/H]_{abs} = -0.90 \pm 0.11$ for this absorber.

Table 2. Morpho-kinematic properties of galaxies detected in both [O III] and CO(1-0) / CO(3–2). Row 1 – properties derived from [O III]: (1) reference name of the galaxy used in this paper, (2) half-light radius, (3) inclination, (4) position angle, (5) maximum velocity, (6) dynamical mass, (7) halo mass. Row 2 – properties derived from CO(1-0) / CO(3–2): (1), (2) half-light radius, (3) inclination, (4) position angle, (5) maximum velocity, (6) dynamical mass, (7) halo mass. Literature references: The values for Q2131−G1 [O III] are taken from Péroux et al. (2017) and the values for Q1130−G2 [O III]/CO and Q1130−G4 [O III]/CO are taken from Péroux et al. (2019).

Galaxy	$r_{1/2,\,[\mathrm{O\,III}]}$ $r_{1/2,\,\mathrm{CO}}$ (kpc)	$i_{[\mathrm{O\,III}]}$ i_{CO} (deg)	$\mathrm{PA}_{[\mathrm{O\,III}]}$ $\mathrm{PA}_{\mathrm{CO}}$ (deg)	$V_{\mathrm{max},\,[\mathrm{O\,III}]}$ $V_{\mathrm{max,\,CO}}$ (km s^{-1})	$\log(M_{\mathrm{dyn},\,[\mathrm{O\,III}]})$ ($\mathrm{M}_\odot$)	$\log(M_{\mathrm{h},\,[\mathrm{O\,III}]})$ ($\mathrm{M}_\odot$)
Q2131−G1	7.9 ± 0.1	60.5 ± 1.2	65 ± 1	200 ± 3	10.87 ± 0.03	11.7 ± 0.1
	$3.7^{+0.5}_{-0.1}$	47^{+10}_{-1}	59 ± 2	195^{+4}_{-30}	–	–
Q1130−G2	14 ± 2	77 ± 2	131 ± 2	264 ± 14	11.3 ± 0.2	12.9 ± 0.1
	2 ± 1	76 ± 3	117 ± 2	134 ± 14	–	–
Q1130−G4	9 ± 2	54 ± 2	86 ± 2	231 ± 12	11.1 ± 0.2	12.7 ± 0.1
	6 ± 1	82 ± 4	84 ± 2	290 ± 19	–	–

∼200 times the critical density of the Universe, is calculated using

$$r_{200} = \left[\frac{M_{200}}{\frac{4}{3}\,\pi\,200\,\rho_{\mathrm{crit}}} \right]^{\frac{1}{3}}, \tag{2}$$

with ρ_{crit} being

$$\rho_{\mathrm{crit}} = \frac{3\,H^2(z)}{8\,\pi\,G}, \tag{3}$$

and using

$$H(z) = H_0 \sqrt{\Omega_M\,(1+z)^3 + \Omega_\Lambda}. \tag{4}$$

Using equations (2)–(4), we compute: $H(z) = 87.9\,\mathrm{km\ s^{-1}Mpc^{-1}}$, $\rho_{\mathrm{crit}} = 437.61\,h^2\,\mathrm{M_\odot\ kpc^{-3}}$, and $r_{200} = 133^{+54}_{-36}$ kpc.

In order to fully describe the NFW mass profile, we compute the concentration parameter (c) which we compute using the redshift-dependent NFW concentration–mass relation from Dutton & Macciò (2014):

$$\log(c) = a + b \times \log(M_{200}/[10^{12} h^{-1}\mathrm{M_\odot}]), \tag{5}$$

with

$$a = 0.520 + (0.905 - 0.520) \times \exp(-0.617 \times z^{1.21}) \tag{6}$$

$$b = -0.101 + 0.026 \times z, \tag{7}$$

and with δ_c being

$$\delta_c = \frac{200}{3} \times \frac{c^3}{\ln(1+c) - \frac{c}{1+c}}. \tag{8}$$

Using our derived M_{200}, we find $c = 7.5^{+0.7}_{-0.7}$ and $\delta_c = 22430^{+4924}_{-4364}$. We calculate the NFW mass profile using

$$M_{\mathrm{DM}}(r) = 4\pi\rho_0 r_{\mathrm{s}}^3 \times \left[\ln\left(1 + \frac{r}{r_{\mathrm{s}}}\right) - \frac{\frac{r}{r_{\mathrm{s}}}}{1 + \frac{r}{r_{\mathrm{s}}}} \right], \tag{9}$$

with $\rho_0 = \delta_{\mathrm{c}}\rho_{\mathrm{crit}}$ and $r_{\mathrm{s}} = \frac{r_{200}}{c}$. The resulting mass profile is shown in Fig. 1. The dark matter mass is in the range of $\log(M_{\mathrm{DM}}(r_{1/2})/\,\mathrm{M_\odot}) = 10.16$–$10.46$ at the [O III] λ5008 emission half-light radius $r_{1/2} = 7.9 \pm 0.1$ kpc.

We calculate the dynamical mass within $r_{1/2}$ using (Epinat et al. 2009)

$$M_{\mathrm{dyn}}(r_{1/2}) = \frac{V^2(r_{1/2})\,r_{1/2}}{G}, \tag{10}$$

with $V(r_{1/2})$ being computed using an arctan velocity profile with the fit parameters derived by GalPak^{3D} using the [O III] λ5008 emission line (Bouché et al. 2015):

$$V(r_{1/2}) = V_{\mathrm{max}}\,\frac{2}{\pi}\,\arctan\left(\frac{r_{1/2}}{r_{\mathrm{t}}}\right), \tag{11}$$

with $r_{\mathrm{t}} = 1.51$ kpc being the turnover radius. The velocity at the half-light radius is therefore $V(r_{1/2}) = 176 \pm 3\,\mathrm{km\ s^{-1}}$ and the dynamical mass at $r_{1/2}$ is $M_{\mathrm{dyn}}(r_{1/2}) = 10.75 \pm 0.3$. Using the dynamical mass and the dark matter mass within the half-light we compute the dark matter fraction within the half-light radius to be $f_{\mathrm{DM}} = 0.24$–0.54.

3.1.4 Morphological and kinematical properties

We first study the morphological properties of Q2131−G1 based on the flux observed with *HST*, MUSE and ALMA. The *HST* image (filter: F702W) of Q2131−G1 with overlaid contours from the observed [O III] λ5008 and CO(3–2) observed flux maps can be found in Fig. 2a). CO(3–2) has a compact and elliptical morphology in the centre of the galaxy with an extent ∼20 kpc. We stress that these higher-z observations would not resolve small-scale clumps as observed in the PHANGS-ALMA survey (Schinnerer et al. 2019). The ionized gas shows a greater extent of ∼40 kpc and has a shape that indicates spiral arms or possible tidal tails (Péroux et al. 2017). There is a region of an [O III] λ5008 flux maximum (at $\sim 21^{\mathrm{h}}31^{\mathrm{m}}35\overset{\mathrm{s}}{.}77$, $-12^\circ 06' 57\overset{''}{.}8$) where CO(3–2) is not detected above the 3σ threshold. This region coincides with a spiral structure in Q2131−G1 and therefore most likely to a region of active star formation. A large fraction of the molecular gas in this region is possibly already depleted due to the star formation process, leading to a CO flux density below the 3σ threshold. The stellar continuum observed by *HST* extends beyond the molecular gas emission above the 3σ threshold.

We study the kinematics of both the ionized and molecular gas of the detected galaxy using the 3D fitting algorithm GalPak^{3D} (Bouché et al. 2015). The algorithm assumes a disc parametric model with 10 free (but also optionally fixable) parameters and probes the parameter space by implementing a Monte Carlo Markov Chain (MCMC) approach with non-traditional sampling laws. The algorithm provides stable results if the signal-to-noise ratio (SNR) per spaxel of the brightest spaxel in the cube is SNR>3. Additionally, the half-light radius has to satisfy the condition $r_{1/2}$/FWHM > 0.75 in order for the algorithm to converge, with the FWHM being the full width at half-maximum of the point spread function (PSF). The $r_{1/2}$/FWHM ratio of Q2131−G1 is below that condition $r_{1/2}$/FWHM ∼0.5, but the algorithm none the less fully converges as we assessed from the MCMC chain. In order to be consistent with the ionized gas kinematic

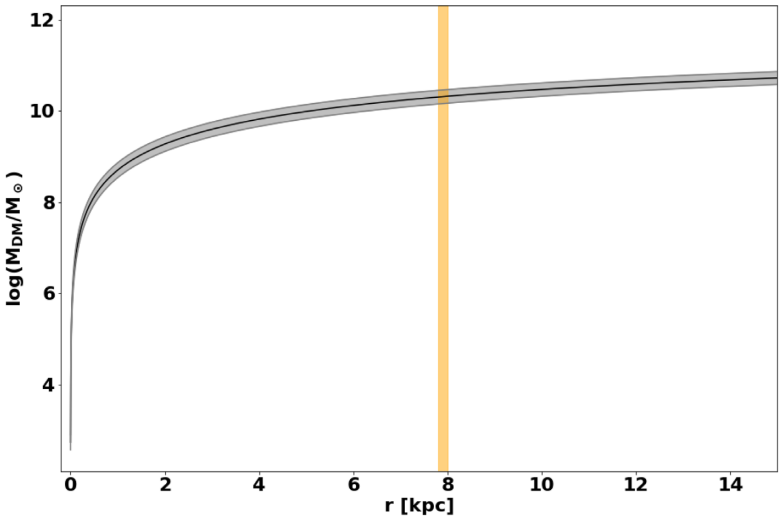

Figure 1. Cumulative mass of the dark matter within Q2131−G1 derived assuming an NFW profile. The shaded regions show the profile for the minimum/maximum derived dark matter mass M_{200}. The vertical orange line marks the [O III] λ5008 half-light radius. The dark matter fraction within the half-light radius is in the range of $f_{\rm DM} = 0.24$–0.53. Therefore, we find the central regions of this galaxy to be baryon dominated.

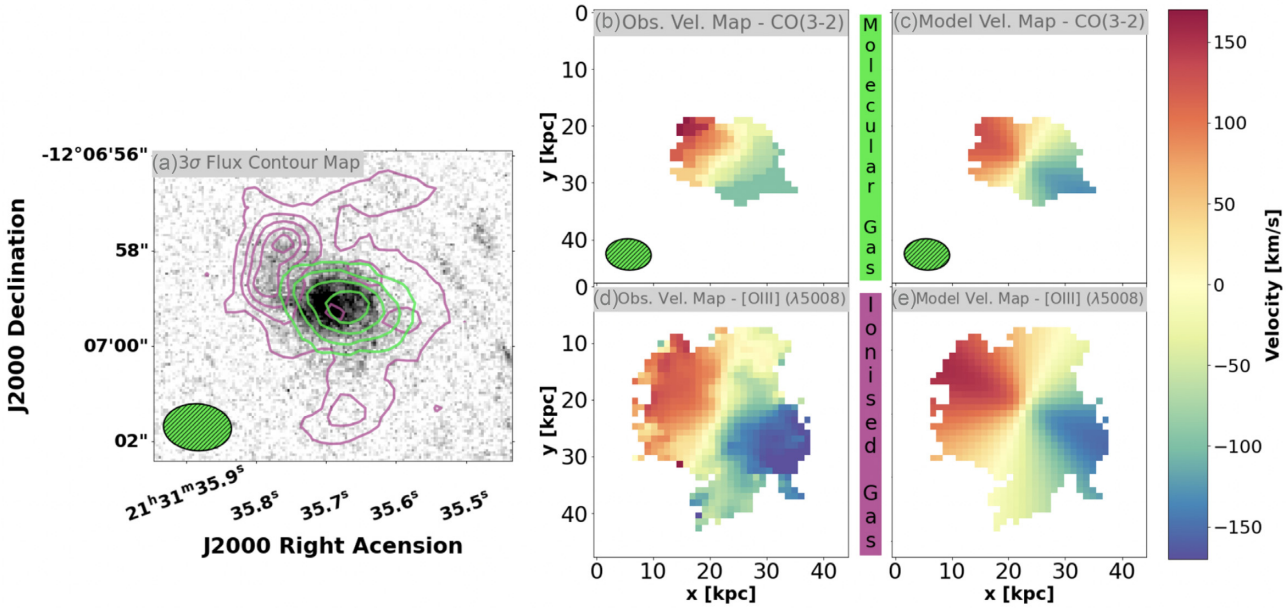

Figure 2. Contour plot and velocity maps of Q2131−G1. Ionized gas contour plot and velocity maps are based on [O III] λ5008. Molecular gas contour plot and velocity maps are based on CO (3–2). (a) *HST* image of Q2131−G1 (detector: PC, filter: F702W, Kacprzak et al. 2015) overlaid with contour plots of the [O III] λ5008 (purple) and CO(3–2) flux using 3σ steps. (b) Observed velocity map of the molecular gas. (c) Model velocity map of the molecular gas. (d) Observed velocity map of the ionized gas. (e) Model velocity map of the ionized gas. In the contour plot a region of high [O III] λ5008 flux is visible where no CO (3–2) is being observed above the 3σ threshold. The direction of rotation for both the ionized and molecular gases is closely correlated and both gas phases show similar maximum rotational velocities.

model used in (Péroux et al. 2017) we also use the exponential flux profile and an arctan velocity profile as assumptions for the disc model. We also ensured that the ALMA cube is in the same reference frame as the MUSE cube (BARY). We additionally create two models with an exponential and tanh velocity profile, which yield different results, in order to take the differences in models into account for the error calculation of the derived properties. The observations are well reproduced by a rotating disc, as can be assessed from the low residuals in the flux (Fig. B2) and velocity residual maps (Fig. B3) in Appendix B.

The morpho-kinematical properties of the ionized gas of Q2131−G1 derived from the [O III] λ5008 and Hβ line in the MUSE observations are described in Péroux et al. (2017). The authors report the following: The maximum circular velocity is well constrained at $V_{\rm max} = 200 \pm 3\,{\rm km\ s^{-1}}$, the half-light radius is found to be $r_{1/2} = 7.9 \pm 0.1$ kpc, the derived position angle is PA $= 65 \pm 1^{\circ}$ and the inclination is $i_{\rm CO} = 60.5 \pm 1.2$. Based on the derived flux, velocity and dispersion maps, Péroux et al. (2017) argue that the galaxy is a large rotating disc, with a velocity gradient along the major axis and a dispersion peak at the centre of the galaxy. Using this approach

we create velocity maps of both the ionized and molecular gas. The observable [(b) ALMA CO(3–2) and (d) MUSE [O III] λ5008)] and model [(c) ALMA CO(3–2) and (e) MUSE λ5008] velocity maps are shown in Fig. 2. We find that the rotational velocities for both the ionized and molecular gas are closely correlated. This is also the case for the model maximum velocities of both components ($V_{\rm max,\,[O\,III]} = 200 \pm 3\,{\rm km\,s^{-1}}$ and $V_{\rm max,CO} = 195^{+4}_{-30}\,{\rm km\,s^{-1}}$). Both of the model velocities are consistent with the observed velocities of both components ($V_{\rm max\text{-}obs,\,[O\,III]} \sim 205\,{\rm km\,s^{-1}}$ and $V_{\rm max\text{-}obs,\,CO} \sim 190\,{\rm km\,s^{-1}}$).

The derived inclination of the molecular and ionized gas in Q2131−G1 are $i_{\rm [O\,III]} = 60.5 \pm 1.2^{\circ}$ and $i_{\rm CO} = 47^{+10^{\circ}}_{-1}$. The position angles (PAs) are PA[O III] $= 65 \pm 1^{\circ}$ and $\rm PA_{CO} = 59 \pm 2^{\circ}$. We conclude that the gas phases in Q2131−G1 are aligned directionally.

While the two models converge in terms of morpho-kinematical properties, they differ in redshifts (CO (3–2): $z_{\rm CO} = 0.42974 \pm 0.00001$, [O III] λ5008: $z_{\rm [O\,III]} = 0.42914 \pm 0.00001$, H$\beta$: $z_{\rm H\beta} = 0.42950 \pm 0.00001$). The other [O III] line in the spectrum is too weak and the [O II] line is disregarded due to its doublet nature. We attribute this discrepancy to a combination of the wavelength calibration uncertainty of MUSE, which translates to a velocity uncertainty of ∼25 km s^{-1}, and an underestimate of the errors provided by GalPak^{3D}. The ALMA frequency accuracy is set by the system electronics and is much better than the corresponding channel width of the cube (50 km s^{-1}). We therefore use the redshift derived from the CO (3–2) model as a zero-point in the analysis of the absorber and gas kinematics. We include the value of $z_{\rm H\beta}$ and other uncertainties mentioned above to estimate an error of ±100 km s^{-1} (∼25 km s^{-1} MUSE velocity uncertainty + ∼75 km s^{-1} kinematical modelling uncertainty) for the kinematic zero-point of the [O III] emission line in the following study of the absorber and gas kinematics. For the CO (3–2) zero-point we estimate an error of ∼75km s^{-1} (kinematical modelling uncertainty).

3.1.5 *Galaxy–gas connection*

Kinematical studies of the gas in the galaxies seen in emission and probed by the quasar sightlines allow us to probe what galaxy/environment the absorbing gas is tracing. We use an approach based on the model rotation curve obtained by GalPak^{3D} to tackle this question.

We extrapolate the rotation curves of Q2131−G1 for both MUSE and ALMA data to the line-of-sight (LOS) towards the quasar to relate it to the gas traced by the H_2 and MgII absorber. The corresponding plots can be found in Fig. 3 where we additionally show the normalized absorption and emission lines with the zero-point of velocity at the redshift of CO (3–2) derived by GalPak^{3D} ($z_0 = 0.42974$). We find the extrapolated velocities of the molecular and ionized of Q2131−G1 between ∼−130 and −135 km s^{-1} and ∼−255 and −275 km s^{-1}. The absorption features, with column densities of $\log(N_{\rm H\,I}/{\rm cm^{-2}}) = 19.5 \pm 0.15$ and $\log(N_{\rm H_2}/{\rm cm^{-2}}) = 16.36 \pm 0.08$ (Muzahid et al. 2016) are found between ∼−60 and + 60 km s^{-1} from the zero-point.

A limit on the CO absorption column density of the absorber Q2131z043$_{\rm H\,I}$ associated with the galaxy Q2131−G1 is calculated following Mangum & Shirley (2015), using an excitation temperature equal to the CMB temperature at the redshift, a 5σ level from the spectrum at the expected position and frequency of the CO(3–2) absorption line as the detection threshold, and an FWHM of 40 km s^{-1} and derive $\log(N_{\rm CO}/{\rm cm^{-2}}) < 14.6$. Using the mean ratio of $N_{\rm CO}/N_{\rm H_2} = 3 \times 10^{-6}$ (Burgh, France & McCandliss 2007), we derive $\log(N_{\rm H_2}/{\rm cm^{-2}}) < 20.1$. This limit is consistent with the value observed from UV wavelength absorption by Muzahid et al. (2016).

Studies of the absorption and emission metallicity connect the absorber to its host. Using a metallicity gradient based on a sample of galaxy–absorber pairs (−0.022 ± 0.004 dex kpc^{-1}, Christensen et al. 2014), we extrapolate the metallicity of Q2131−G1 to the LOS towards the quasar. We take into account the observed flattening of the oxygen metallicity gradient beyond $2 \times r_{1/2}$ (Sánchez-Menguiano et al. 2016) and assume that there is no change in the metallicity of the galaxy between $2 \times r_{1/2} = 15.8 \pm 0.2$ kpc and the impact parameter $b = 52$ kpc. We use 12+log(O/H) = 8.98 ± 0.02 by Péroux et al. (2017) as the metallicity of the galaxy, including the value by Muzahid et al. (2016; 12+log(O/H) = 8.68 ± 0.09) in the error calculation. The extrapolated metallicity of Q2131−G1 at the impact parameter (b = 52 kpc) is $Z_{\rm em} = -0.06^{+0.09}_{-0.62}$. We additionally use an alternative metallicity gradient of $0.1/r_{1/2}$ (which in the case of Q2131−G1 translates to 0.01266 ± 0.00016 dex kpc^{-1}) derived by the CALIFA survey (Sánchez et al. 2014) and find the extrapolated metallicity of Q2131−G1 at the impact parameter to be $Z_{\rm em} = 0.09^{+0.02}_{-0.48}$. Literature provides metallicity measurements using various species: $[{\rm Fe/H}]_{\rm abs} > -0.96$ from Hamanowicz et al. (2020), $[{\rm O/H}]_{\rm abs} = -0.26 \pm 0.19$ using ionization modelling from Muzahid et al. (2016), and the ionization corrected metallicity of $[{\rm S/H}]_{\rm abs} > -0.72$ (originally reported as $[{\rm S/H}]_{\rm abs} > -0.40$ assuming $\log(N_{\rm H\,I,\,abs}/{\rm cm^{-2}}) = 19.18$ instead of 19.5) by Som et al. (2015). The global dust-free metallicity is $[{\rm X/H}]_{\rm abs} = -0.54 \pm 0.18$ (Péroux et al. 2017). We find that both of the extrapolated metallicities are consistent with each other and consistent with the metallicity derived by Péroux et al. (2017).

3.2 Limits from non-detections

For the fields Q1232−0224, Q0152−2001, and Q1211−1030 with no CO detected counterparts in emission to the galaxies observed with MUSE and *HST*, we derive limits on the molecular mass and depletion times.

For each cube we consider an ellipsoidal area with the minor axis, position angle and FWHM of the synthesized beam centred around the expected position of the galaxy with the frequency range being set to ±100 km s^{-1} centred around the redshifted frequency of the CO(3–2) emission line. We then assume the emission spectrum to be a Gaussian with an amplitude set to the RMS of the ellipsoidal area and an FWHM of 200 km s^{-1}. The flux limit is then the area under this line within the 5σ range.

We calculate the mass limits and depletion times following the same prescription as described in Section 3.1.1 [namely following Solomon et al. (1992), Fixsen et al. (1999), and Genzel et al. (2015)] and equation (1). The molecular gas mass limits use an $\alpha_{\rm CO}$ conversion factor based on the lowest measured metallicity of the galaxy to provide conservative limits of both the molecular gas mass and depletion time.

The results for the CO flux, luminosity, mass, and depletion time limits for Q0152−G1, Q1211−G1, and Q1232−G1 can be found in Table 1. The CO(1–0) limits on the luminosity $L_{\rm CO}$ are of the order $L_{\rm CO} \sim 10^8$ K kms^{-1}pc^2, which fits the sensitivity estimates based on the ALMA sensitivity calculator calculated for our observations at $z \sim 0.4$. Our limits are more stringent than similar observations studying the molecular gas in objects associated with absorbers [e.g. MEGAFLOW by Freundlich et al. (2021), targeting galaxies around Mg II absorbers, or Kanekar et al. (2018, 2020)], which are sensitive to luminosities $L_{\rm CO} > \sim 10^9$ K kms^{-1}pc^2. The molecular gas mass

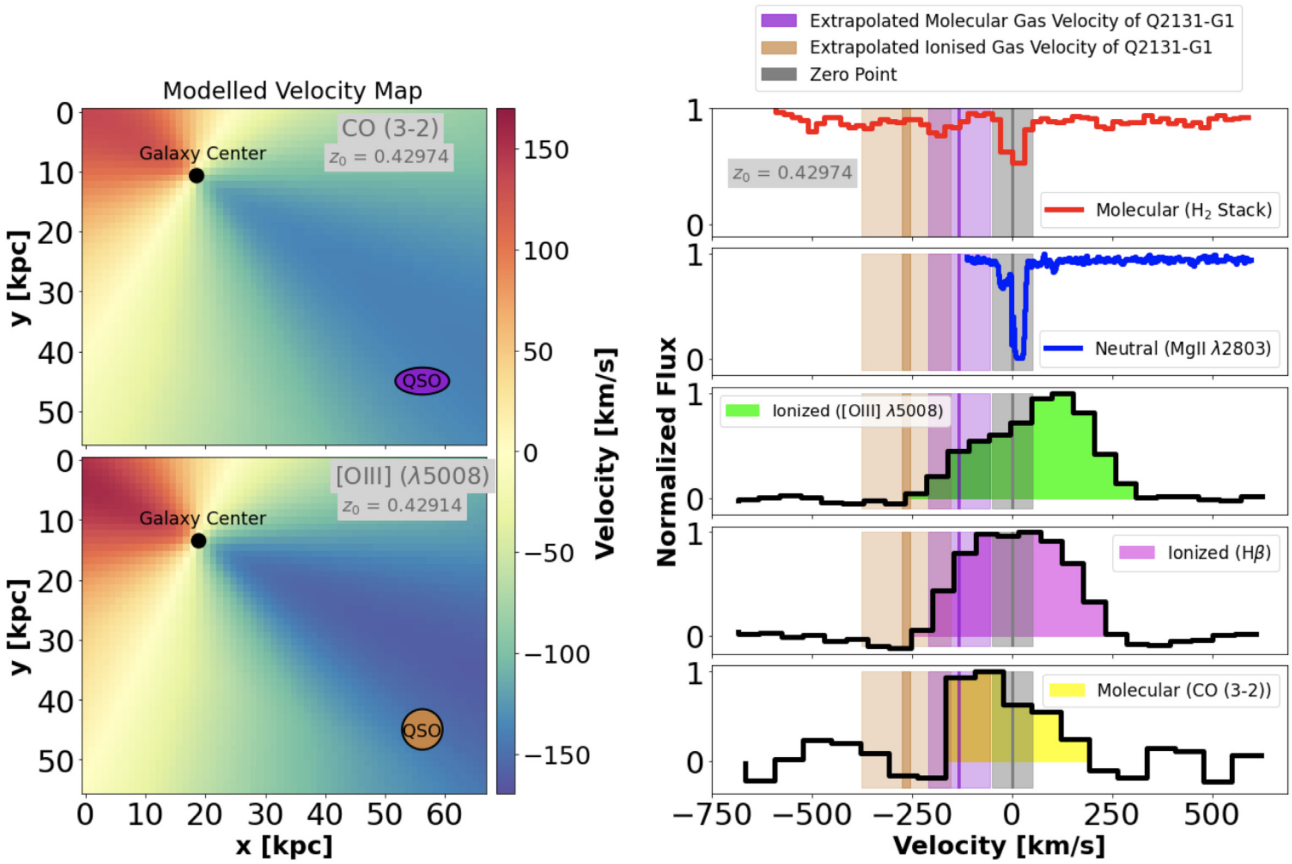

Figure 3. Extrapolated model velocity maps and normalized flux of the Mg II (λ2803) and stacked H_2 absorption line and [O III] λ5008, H β, CO(3–2) emission lines. The velocity zero-point of the spectra is set to the redshift of CO (3–2) derived from the kinematic study ($z_0 = 0.42974$; displayed as the grey shaded area). The magenta and brown bars display the extrapolated velocities of the molecular and ionized gas of Q2131−G1 respectively. The shaded magenta and brown bars display the errors of the extrapolated velocities (75 km s^{-1} for the molecular gas, 100 km s^{-1} for the ionized gas). Extrapolating the model velocity maps derived from GalPak^{3D} to the line of sight toward the quasar show that at the position of the quasar the molecular and ionized gases of Q2131−G1 are located between ∼−130 and −135 km s^{-1} and ∼−255 and −275 km s^{-1} respectively, while the absorption features are found between ∼−60 and + 60 km s^{-1}. We thus conclude that the two-component absorption features are consistent with in part an extended rotating disc of Q2131−G1 and in part gas falling on to Q2131−G1.

limits are in the range of $M_{\rm mol} \sim (2.8–18.3) \times 10^9\,{\rm M}_\odot$ and the depletion time limits are in the range of $\tau_{\rm dep} \sim 1.4–37$ Gyr.

4 DISCUSSION

The multiwavelength approach in this work allows us to closely study the different gas phases within and around H I-selected galaxies. *HST* spectroscopy provides neutral and molecular gas information through absorption while MUSE and ALMA observations enable us to study the ionized and molecular gas content through emission. In this section we provide a detailed discussion of the observed properties and how they compare to current observations.

4.1 Strongly coupled gas phases within a rotating disc

Recent observations of the ionized and molecular gas phases in galaxies between redshifts $z \sim 0.1–1.4$ have found that both phases mostly align well directionally (e.g. Møller et al. 2017; Klitsch et al. 2018; Übler et al. 2018; Loiacono et al. 2019; Molina et al. 2019, 2020; Péroux et al. 2019). Similarly, we find that Q2131−G1 is well constrained by a disc model and that the ionized and molecular gas phases are aligned well directionally with similar inclinations and position angles.

We also find a similar maximum rotational velocity ($V_{\rm max} \sim 200$ km s^{-1}) of the molecular and ionized gas within Q2131−G1. This is consistent with the EDGE-CALIFA survey (Levy et al. 2018), where ionized and molecular gas kinematics (traced by Hα) were compared in local galaxies. While the survey does find that for the majority of galaxies the rotational velocity measured from the molecular gas is higher than that from the ionized gas, there are cases where similar rotational velocities for both phases have been observed.

Due to the good alignment of the ionized and molecular gas phase, both directionally and rotationally, we find that the two gas phases are strongly coupled within Q2131−G1.

4.2 Identifying the disc tilt

Kinematic modelling provides the inclinations of both gas phases, but these values are degenerate without knowing the tilt of the disc. A proposed solution to breaking the degeneracy of the disc tilt is to use the rotation curve and the winding direction of spiral arms (Martin et al. 2019). Based on the likely assumption that in a self-

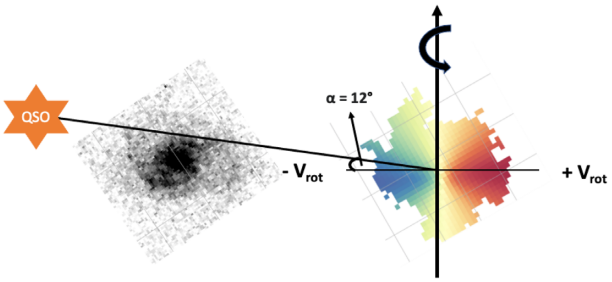

Figure 4. Sketch of the QSO–galaxy plane for identifying the disc tilt. The galaxy is rotated in order to align the major axis with the x-axis in the sketch. The spiral arms of Q2131−G1 wind in the opposite direction of the galaxies rotation and we conclude that the inclination has a negative sign.

gravitating, collisionless system only trailing spiral patterns are long lived (Carlberg & Freedman 1985) and most spiral patterns therefore lag behind the direction of rotation with increasing radius, depending on the winding rotation, one can infer a positive or negative sign of the inclination. The winding rotation of the spiral arms in Q2131−G1 observed in the *HST* image are opposite to the direction of rotation of the galaxy and the inclination therefore has a negative sign (see Fig. 4).

4.3 Gas probed in absorption connected to a rotating disc and infalling gas

Previous authors state that an individual absorber is sometimes associated with multiple galaxies (Hamanowicz et al. 2020). In particular, in the field Q2131−1207 four galaxies are found at the same redshift and physically close to the absorber, indicating that Q2131−G1, found at $b = 52$ kpc, is part of a group environment. Kinematical studies of the gas phases and the absorption features help alleviate these ambiguities studying how the different components relate in velocity space (see e.g. Rahmani et al. 2018a)

To relate the gas probed in absorption with the absorber host we extrapolate the model rotation curve towards the sightline of the quasar in Section 3.1.5 (see Fig. 3). We find that the velocities of the ionized and molecular gases of Q2131−G1 at the point of the quasar sightline are blueshifted compared to the systemic redshift. A two-component absorption is found between ∼−60 and 60 km s^{-1}. Due to the low azimuthal angle (12° ± 1°) of Q2131−G1 (Péroux et al. 2017) and simulations indicating that outflowing gas preferentially leaves the galaxy in a conical shape along its minor axis (Brook et al. 2011; Péroux et al. 2020), we assume an outflow scenario to be unlikely for both absorption components.

The weaker component is rotating in the same direction as the galaxy at less negative velocities. Further, the extrapolated metallicities of Q2131−G1 ($Z_{\rm em} = -0.06^{+0.09}_{-0.62}$ and $Z_{\rm em} = 0.09^{+0.02}_{-0.48}$, depending on the metallicity gradient used) at the LOS towards the quasar indicate a connection between the gas probed in absorption and emission as it is consistent with the absorber metallicity ($[{\rm X/H}]_{\rm abs} = -0.54 \pm 0.18$). The extrapolated velocities and metallicities of the galaxy and the weaker absorption component are therefore consistent with being part of an extended rotating disc.

The stronger absorption component is redshifted compared to the systemic redshift. Gas rotating with the disc of the galaxy is expected to have blueshifted velocities, making the stronger absorption component inconsistent with being part of the extended rotating disc. Further, the low azimuthal makes it a likely inflow (e.g. Bordoloi et al. 2011; Stewart et al. 2011; Shen et al. 2012). The metallicity difference between the Q2131−G1 and the absorber lies in the infalling section of the galaxy to gas metallicity versus azimuthal angle plot seen in Péroux et al. (2016; fig. 8 in the publication). Based on the metallicity difference and the geometry and orientation arguments, the stronger component is consistent with being gas falling on to Q2131−G1. We note that current data does not exclude that the gas could potentially also be falling on to Q2131−G2. The H_2 column density of the absorber also poses the question if and how it is possible to have a considerable molecular gas phase, with temperatures down to 10 K, in infalling gas.

We thus conclude that the two-component absorption features are consistent with in part an extended rotating disc of Q2131−G1 and in part gas falling on to Q2131−G1.

4.4 Specifics of H I-selected systems

Previous studies of H I-selected systems have observed gas depletion times that are a few times longer than what is typically found in surveys of emission-selected galaxies (see especially Kanekar et al. 2018). This poses the question whether the H I-selection preferentially selects galaxies that have large gas reservoirs for their SFR. We compare the detected galaxy Q2131−G1 with two current emission-selected molecular gas surveys, namely xCOLD GASS (e.g. Saintonge et al. 2017) and the PHIBSS 1 & 2 surveys (e.g. Tacconi et al. 2018) of galaxies at redshift $z < 1.1$. We additionally contrast with previously published H I-selected galaxies where molecular masses, stellar masses and SFR have been measured. We use a metallicity-dependent $\alpha_{\rm CO}$ conversion factor for the comparison sample if metallicity information is provided (namely Papadopoulos et al. 2012; Bolatto et al. 2013; Genzel et al. 2015). Otherwise we use $\alpha_{\rm CO} = 4.3 {\rm M}_\odot ({\rm K\,km/s\,pc})^{-1}$ from Bolatto et al. (2013) or in the case of Klitsch et al. (2018), $\alpha_{\rm CO} = 0.6 {\rm M}_\odot ({\rm K\,km/s\,pc})^{-1}$ from Papadopoulos et al. (2012) is used because there is evidence that this galaxy is a luminous infrared galaxy (LIRG). In the case of the MUSE-ALMA haloes sample the SFR is not dust corrected (with exception of the field Q1130−1449), therefore the SFR can be considered as a lower limit.

Fig. 5 shows the SFR, molecular mass and depletion times of the emission and H I-selected galaxies. Q2131−G1 (star symbol) is comparable to the galaxies of the mass-selected xCOLD GASS and PHIBSS 1 & 2 galaxies, as it lies within the $M_{\rm mol}$–SFR, $M_\star$–$M_{\rm mol}$ and $M_\star$–SFR planes. While Q2131−G1 fits well in the $M_{\rm mol}$–SFR plane, it is on the lower side of the derived SFR of comparable molecular masses, comparable to other galaxies associated with sub-DLAs. The deviations from the $M_{\rm mol}$–SFR plane are especially drastic in the case of galaxies associated with DLAs, which implies that H I-selection traces objects that have large gas reservoirs (at given SFR). Similarly the depletion time-scale of Q2131−G1, Q1130−G2, and Q1130−G6 are an order of ∼2–53 larger than the median for emission-selected galaxies in the xCOLD GASS and PHIBSS survey with $\tau_{\rm dep,\,med} \approx$ 1.0 Gyr and ≈0.7 Gyr, respectively.

Studying this trend is limited due to the low number of molecular gas and star formation rate observations of H I-selected galaxies. Further studies will test whether H I-selection preferentially selects galaxies that have large molecular gas reservoirs for their given SFR.

4.5 Connecting galaxy properties with gas properties

One key objective in studying absorption-selected galaxies is associating absorbers with potential absorber hosts and connecting absorber properties to the low density gas found by absorption. We compare the derived molecular gas mass of Q2131−G1 and the H I column

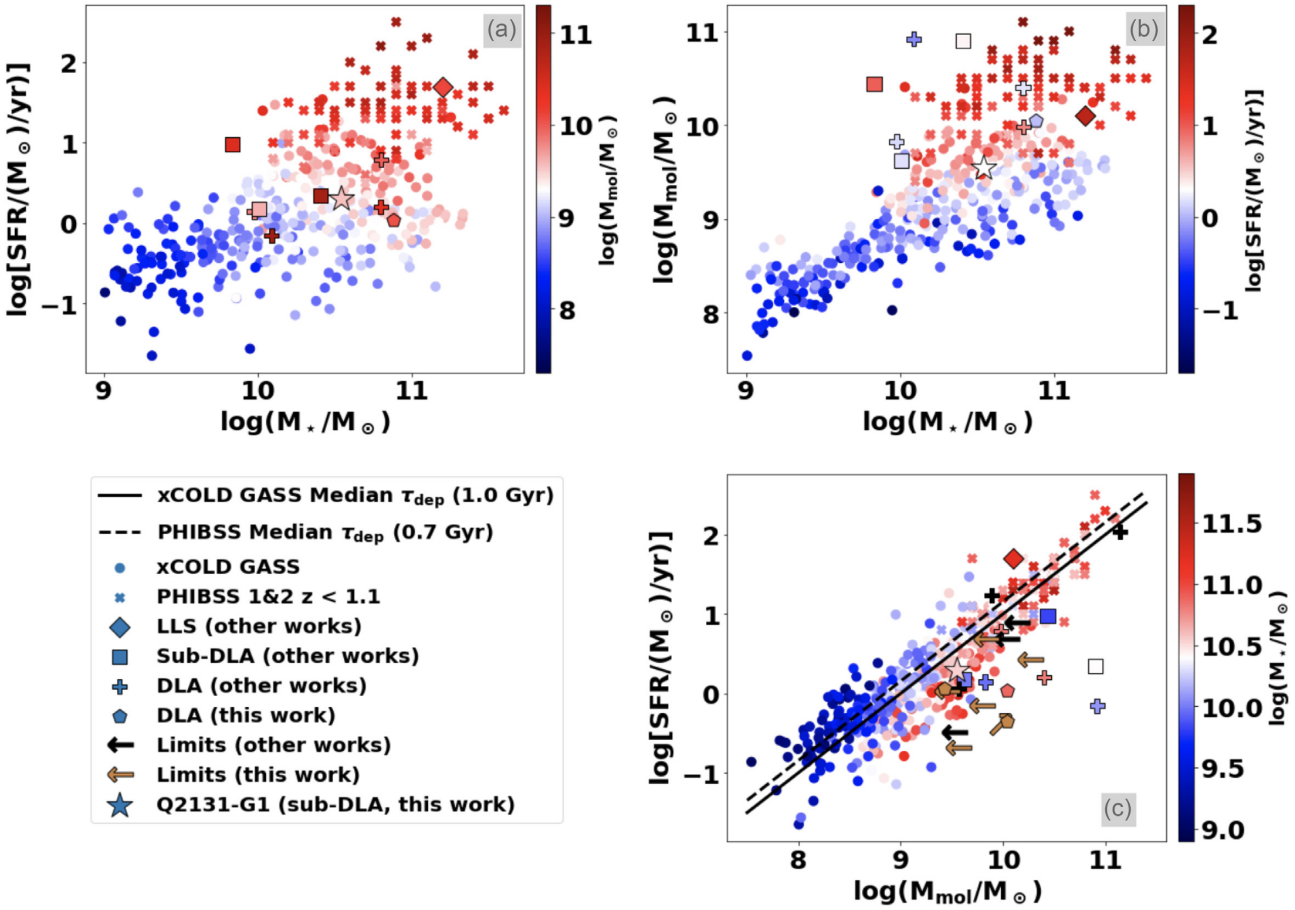

Figure 5. Star formation rate (SFR), molecular mass ($M_{\rm mol}$), and depletion time ($\tau_{\rm dep}$) plotted for H I-selected galaxies, the xCOLD GASS and PHIBSS 1&2 survey (at $z < 1.1$). H I-selected galaxies with molecular gas mass limits as well as galaxies without stellar mass data are additionally plotted in the SFR–$M_{\rm mol}$ plot and have a black (other works) / brown (this work) colour. The median depletion time for xCOLD GASS ($\tau_{\rm dep} = 1.0$ Gyr; Saintonge et al. 2017) and PHIBSS ($\tau_{\rm dep} = 0.7$ Gyr; Tacconi et al. 2018) are plotted as a black (dashed) line. Q2131−G1 lies within the $M_{\rm mol}$–SFR, $M_\star$–$M_{\rm mol}$, and $M_\star$–SFR planes of the xCOLD GASS and PHIBSS 1&2 surveys. We note that the SFR of Q2131−G1 is not dust corrected and therefore should be considered as a lower limit. The molecular gas mass for the majority of sub-DLAs and DLAs for their given SFR is found to be higher than for emission-selected samples. This leads to depletion times in H I-selected galaxies that are up to multiple factors higher than for emission selected galaxies. This implies that selection based on strong H I absorbers traces objects that have large gas reservoirs (at given SFR). Literature references: xCOLD GASS: Saintonge et al. (2017); PHIBSS: Tacconi et al. (2018); LLS (other works): Klitsch et al. (2018); sub-DLA (other works): Kanekar et al. (2018), Neeleman et al. (2016); DLA (other works): Kanekar et al. (2018), Møller et al. (2017), Neeleman et al. (2018); Limits (other works): Klitsch et al. (2018), Kanekar et al. (2018).

density of the associated absorber Q2131z043$_{\rm H\,I}$ with previously detected H I absorbers and associated absorber hosts detected in CO in Fig. 6. In order to provide a fair comparison, we use the same conversion factors as described in Section 4.4.

Molecular gas in H I-selected systems is found in systems with H I column densities between $\log(N_{\rm H\,I}/{\rm cm}^{-2}) \sim 18$–22, from Lyman-limit systems (Klitsch et al. 2018) to sub-DLAs (this work; Neeleman et al. 2016; Kanekar et al. 2018) and DLAs (Møller et al. 2017; Kanekar et al. 2018; Neeleman et al. 2018; Péroux et al. 2019; see Fig. 6). The molecular masses detected span over a large range of $\log(M_{\rm mol}/{\rm M}_\odot) \sim 9.5$–11.3. The lower end of this range is typically for the detection limit of the observations. It is interesting to note that H I-selection can be associated with such large molecular gas reservoirs, but no correlation between the H I absorption column density and the absorber host molecular mass is seen.

The most similar counterpart to Q2131−G1 is the galaxy associated with the absorber at redshift $z = 0.101$ in the quasar spectrum of PKS 0439−433 (Neeleman et al. 2016). While the absorber metallicity in PKS 0439−433 is higher ([S/H]= 0.1, Som et al. 2015), both absorbers show an H I-column density of $\log(N_{\rm H\,I}/{\rm cm}^{-2}) \sim 19.5$ and the associated galaxies have closely matching molecular masses of $\log(M_{\rm mol}/{\rm M}_\odot) \sim 9.6$. Additionally, both absorber systems have H_2 absorption features with H_2 column densities of $\log(N_{\rm H_2}/{\rm cm}^{-2}) \sim 16.5$. The calculated limit on the CO column density ($\log(N_{\rm CO}/{\rm cm}^{-2}) < 14.6$) in Section 3.1.5 and the subsequently derived limit on the H2 column density ($\log(N_{\rm H_2}/{\rm cm}^{-2}) < 20.1$) is consistent with the detected H_2 column density. The galaxy in Neeleman et al. (2016) does have a lower impact parameter of ∼20 kpc than Q2131−G1 ($b = 52$ kpc), but the absorption features cannot be kinematically associated to the rotating disc of the absorber host or infalling gas and is likely part of the CGM of the galaxy. While we might probe different environments, the similarity of the molecular masses in the absorber hosts and the H I/H_2 column densities of the absorbers indicate a connection of these parameters. The other galaxies in this sample either lack observations of possible H_2 absorption features, or have not been detected at all. This is partly due to the low detection rates of H_2 in quasars [∼16 per cent for high-z absorbers (Noterdaeme et al. 2008), ∼50 per cent for low-z absorbers (Muzahid, Srianand &

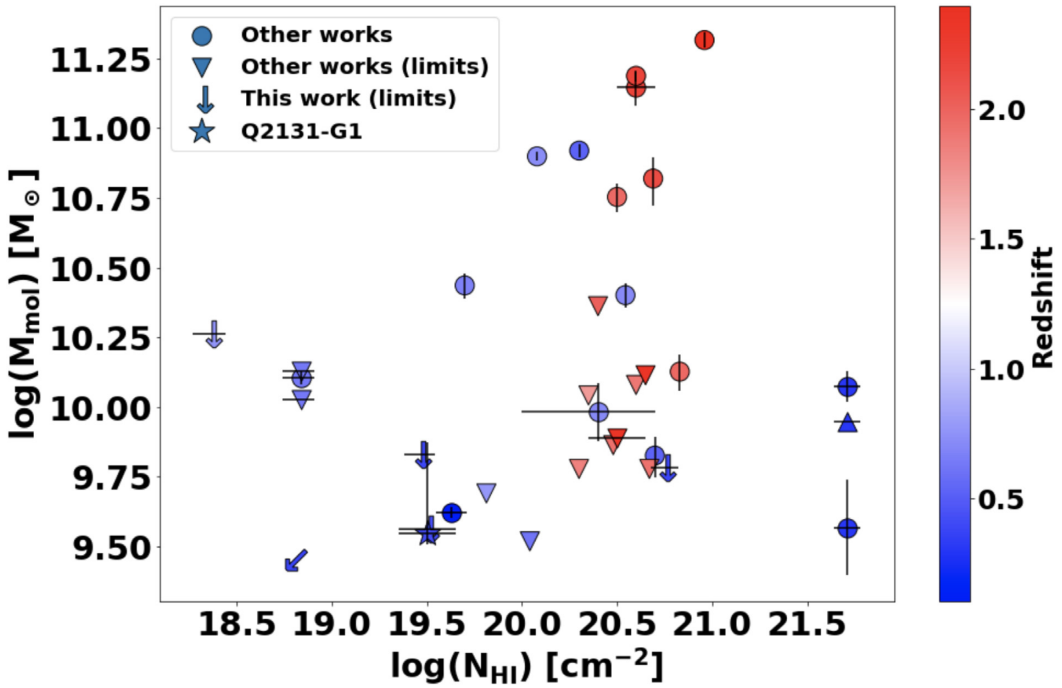

Figure 6. Absorber H I column density plotted against the molecular mass (limits) of absorber hosts by various published works (Neeleman et al. 2016; Møller et al. 2017; Augustin et al. 2018; Kanekar et al. 2018; Klitsch et al. 2018; Neeleman et al. 2018; Péroux et al. 2019; Kanekar et al. 2020). Q2131−G1 is on the lower side of previously detected molecular masses in H I absorption selected galaxies.

Charlton 2015)]. Nonetheless, future studies of molecular gas in both absorbers and absorber hosts, combined with kinematic studies that help to associate these systems are essential for studying a possible connection between the high density molecular gas found in galaxies and the low density molecular gas found in absorbers.

4.6 A dark matter fraction evolving with redshift

Current extragalactic surveys of the dark matter fraction in the central regions of galaxies provide evidence for a dark matter fraction evolution with redshift, with the dark matter fraction declining for higher redshifts (e.g. Genzel et al. 2020; Price et al. 2020). A possible explanation for this evolution of the dark matter fraction over different redshifts is given by the IllustrisTNG (TNG) simulations (Lovell et al. 2018). The authors find that the evolution is due to the more centrally concentrated baryonic mass at higher redshift galaxies. They also show that this evolution is highly aperture dependent. Using a fixed physical aperture for all galaxies, in their case 5 kpc, leads to a dark matter fraction that is almost constant over time. Using the stellar half-mass radius instead reveals the evolution of the dark matter fraction with redshift. This is especially evident for galaxies in the $10^{11}M_{\odot}$ stellar mass regime, which are highly concentrated at high redshifts. At a fixed stellar mass these galaxies show a substantial increase in size, leading to smaller half-mass radii at higher redshifts.

Observationally, various surveys provide some constraints of the dark matter fraction at different redshifts. The DiskMass survey of local galaxies finds that the central dark matter fractions are in the range of 0.5–0.9 within 2.2 times the disc scale radius, which corresponds to ∼1.6 times the half-light radius (Martinsson et al. 2013). The SWELLS survey (Barnabè et al. 2012; Dutton et al. 2013; Courteau & Dutton 2015) finds lower dark matter fractions in the range of 0.1 - 0.4 using the same aperture. This discrepancy is most likely due to the SWELLS galaxies having larger bulge components than the DiskMass survey. Galaxies in the redshift range $z = 0.6$ - 1.2 show a median of $f_{\rm DM} \sim 0.3$, while galaxies in the redshift range $z = 1.2$–2.5 have a median of $f_{\rm DM} \sim 0.12$ within the half-light radius (Genzel et al. 2020). For higher redshifts the dark matter fraction goes as low as $f_{\rm DM} = 0.05$ (Price et al. 2020) within the half-light radius.

In Q2131−G1 we find a dark matter fraction within the half-light radius of $f_{\rm DM} = 0.24$–0.54. We therefore find that the central regions of this galaxy are dominated by baryons. Compared to the surveys and simulations, Q2131−G1 fits well between the dark matter fractions found in the DiskMass survey and is also consistent with the median of galaxies observed in the redshift range 0.6–1.2. It is also within the range of galaxies observed within the SWELLS survey. The dark matter fraction is comparable to the one found in galaxies in TNG at the stellar mass $M_{\star} = 10^{10.5}M_{\odot}$ at redshift $z = 2$. While the redshift of these galaxies in TNG is higher than of Q2131−G1, the galaxies within the SWELLS survey fit into the same regime of galaxies found in TNG. Therefore, this discrepancy could partly also be due to Q2131−G1 possibly having a significant bulge component.

4.7 CO detection rate of MUSE-ALMA haloes survey

We target the CO(3–2) line of nine galaxies associated with six absorbers with ALMA and detect four of them (∼45 per cent detection rate). All of the non-detected galaxies have metallicities below 12 + log(O/H) ∼ 8.65. Four of the non-detected galaxies have sub-solar metallicities of 12 = log(O/H) <8.32, but have higher molecular gas mass limits than the detected galaxy Q2131−G1. Molecular gas in galaxies with sub-solar gas phase metallicity is shown to be deficient in CO, due to the CO molecule being photodissociated at larger fractions compared to higher metallicity galaxies (Wolfire, Hollenbach & McKee 2010; Bolatto et al. 2013). This in turn leads

to a lower observed CO flux density and longer integration times are needed for observing low metallicity galaxies in CO. We therefore attribute these non-detection to the low metallicities of the galaxies.

5 CONCLUSION

In this paper, we present MUSE and new ALMA observations of the fields Q2131−1207, Q0152−2001, Q0152−2001, Q1211+1030 with LLS, sub-DLAs, and DLAs at $z \sim 0.4$ and $z \sim 0.75$. We also include the previously published field Q1130−1449 with three CO-detected galaxies ($z \sim 0.3$) in our analysis (Péroux et al. 2019). We detect one counterpart (Q2131−G1) of a previously detected (*HST* and MUSE) galaxy with ALMA observing the CO(3–2) emission line in the field Q2131−1207. We analyse the morphological, kinematical and physical properties of Q2131−G1 with a focus on the molecular gas content. For the non-detections we provide limits on the molecular gas mass and depletion time.

The findings can be summarized as follows:

(i) The ionized gas phase in Q2131−G1 has a shape indicating spiral arms and possible tidal tails from previous interactions and an extent of ∼40 kpc. The molecular gas is found in a more compact and elliptical morphology of smaller extent (∼20 kpc). The extent of the stellar continuum is in between the ionized and molecular gas phase.

(ii) Using the sophisticated 3D forward modelling tool GalPak^{3D} we study the kinematics of the ionized and molecular gas phase of Q2131−G1. We assume a disc model with an exponential flux profile and a tanh rotation curve for both gas phases and find that the gas phases align well directionally with similar inclinations ($i_{[\mathrm{O\,III}]} = (60.5 \pm 1.2)^\circ$, $i_{\mathrm{CO}} = (47^{+10}_{-1})^\circ$) and position angles ($\mathrm{PA}_{[\mathrm{O\,III}]} = (65 \pm 1)^\circ$, $\mathrm{PA}_{\mathrm{CO}} = (59 \pm 2)^\circ$). The maximum rotational velocity is equal for both gas phases ($V_{\mathrm{max}} \sim 200\,\mathrm{km\,s^{-1}}$). This is consistent with findings by the EDGE-CALIFA survey (Levy et al. 2018), where a fraction of 25 per cent of their sample contained galaxies with equal maximum velocities. We therefore conclude that the ionized and molecular gas phase are strongly coupled within Q2131−G1.

(iii) The absorber shows a neutral and molecular absorption two-component profile, with the weaker component blueshifted and the stronger component redshifted compared to the systemic redshift derived from the kinematic model of the CO emission. Extrapolating the model velocity maps towards the line of sight of the quasar shows that the weaker absorption component is consistent with being part of the extended rotating disc of Q2131−G1. Thanks to metallicity, geometry and orientation arguments, we find that the stronger component is consistent with being gas falling on to Q2131−G1. The considerable amount of molecular gas traced by the absorber poses the question of the presence of a molecular cold phase in infalling gas.

(iv) The molecular mass ($M_{\mathrm{mol}} = 3.52^{+3.95}_{-0.31} \times 10^9\,\mathrm{M}_\odot$) is on the low end of previously detected H I-selected galaxies. A similar counterpart, associated with the absorber at redshift $z = 0.101$ in the quasar spectrum of PKS 0429−433 (Neeleman et al. 2016), interestingly has a similar molecular mass and shows roughly the same H I column density ($\log(N_{\mathrm{H\,I}}/\mathrm{cm}^{-2}) \sim 19.5$) and H_2 column density ($\log(N_{\mathrm{H_2}}/\mathrm{cm}^{-2}) \sim 16.5$). While the absorption was attributed to the CGM of the galaxy and not being part of the rotating disc or infalling gas, the similarities of these properties are striking. We conclude that future studies of molecular gas in both absorbers and absorber hosts are essential to studying a possible connection of these properties.

(v) We compute a dark matter fraction within the half-light radius of $f_{\mathrm{DM}} = 0.24$–0.54, showing that the inner parts of the galaxy are baryon dominated. The dark matter fraction fits between the dark matter fraction of the DiskMass survey ($f_{\mathrm{DM}} \sim 0.5$–0.9, Martinsson et al. 2013) and the median dark matter fractions observed in the redshift range $z = 0.6$–1.2 ($f_{\mathrm{DM}} \sim 0.3$, Genzel et al. 2020), providing a further indicator for a redshift evolution of the dark matter fraction.

(vi) The depletion times (including upper limits) of our sample are in the range of ($\tau_{\mathrm{dep}} \sim 1.4$–$37$ Gyr). The depletion times of the CO-detected galaxies Q2131−G1, Q1130, and Q1130−G6 are an order of ∼2–53 times larger than the median depletion time for emission-selected galaxies in the xCOLD GASS (Saintonge et al. 2017) and PHIBSS (Tacconi et al. 2018) samples. This result is consistent with previously detected H I-selected galaxies which also showed higher depletion times compared to emission selected samples. The high depletion times are a consequence of the high molecular gas masses of H I-selected galaxies for their low SFR. We therefore conclude that H I-selected galaxies possibly preferentially select galaxies that have large molecular gas reservoirs for their low SFR, while a complete picture of the H I-selected population should be obtained by following up the non-detected galaxies for further studies of this possible selection bias.

(vii) The five non-detected galaxies all have metallicities below $12 = \log(\mathrm{O/H}) \sim 8.65$. Four of the non-detected galaxies have low sub-solar metallicities of $12 = \log(\mathrm{O/H}) < 8.32$, but have higher molecular gas mass limits than the detected galaxy Q2131−G1. Combined with the evidence that CO is photodissociated at larger fractions in low-metallicity galaxies compared to higher metallicity galaxies (Wolfire et al. 2010; Bolatto et al. 2013) and therefore having a lower CO flux density leads to the conclusion that one should account for a higher integration time when observing CO in subsolar metallicity galaxies.

ACKNOWLEDGEMENTS

We thank the anonymous referee for the very helpful and detailed comments which helped to improve the final version of the manuscript. We want to thank the ALMA staff for performing the observations. This paper makes use of the following ALMA data: ADS/JAO.ALMA#2017.1.00571.S. ALMA is a partnership of ESO (representing its member states), NSF (USA) and NINS (Japan), together with NRC (Canada), MOST and ASIAA (Taiwan), and KASI (Republic of Korea), in cooperation with the Republic of Chile. The Joint ALMA Observatory is operated by ESO, AUI/NRAO, and NAOJ. Based on observations made with the NASA/ESA *Hubble Space Telescope*, and obtained from the Hubble Legacy Archive, which is a collaboration between the Space Telescope Science Institute (STScI/NASA), the Space Telescope European Coordinating Facility (ST-ECF/ESA), and the Canadian Astronomy Data Centre (CADC/NRC/CSA). We thank Nicolas Bouché for developing and distributing the GalPak^{3D} algorithm and for the interactions on the GalPak^{3D} algorithm. RS thanks ESO and the IMPRS program for the support of his PhD. AK gratefully acknowledges support from the Independent Research Fund Denmark via grant number DFF 8021-00130. VPK gratefully acknowledges support from NASA grant 80NSSC20K0887 and US NSF grant AST/2007538. RA was supported by NASA grants 80NSSC18K1105 and HST GO # 15075.

DATA AVAILABILITY

Used VLT/MUSE data are available through the ESO Science Archive Facility (http://archive.eso.org/cms.html), ALMA data are available through the ALMA Science Archive (https://almascience.eso.org/asax/), and *HST* data are available through the Hubble Legacy

Archive (https://hla.stsci.edu). The corresponding IDs are noted in Section 2.

REFERENCES

Anderson M. E., Bregman J. N., 2010, ApJ, 714, 320
Anderson M. E., Bregman J. N., Dai X., 2013, ApJ, 762, 106
Augustin R. et al., 2018, MNRAS, 478, 3120
Augustin R. et al., 2019, MNRAS, 489, 2417
Barnabè M. et al., 2012, MNRAS, 423, 1073
Behroozi P. S., Conroy C., Wechsler R. H., 2010, ApJ, 717, 379
Bergeron J., 1986, A&A, 155, L8
Bish H. V., Werk J. K., Prochaska J. X., Rubin K. H. R., Zheng Y., O'Meara J. M., Deason A. J., 2019, ApJ, 882, 76
Boissé P., Le Brun V., Bergeron J., Deharveng J.-M., 1998, A&A, 333, 841
Bolatto A. D., Wolfire M., Leroy A. K., 2013, ARA&A, 51, 207
Bordoloi R. et al., 2011, ApJ, 743, 10
Bouché N. et al., 2012, MNRAS, 419, 2
Bouché N., Carfantan H., Schroetter I., Michel-Dansac L., Contini T., 2015, AJ, 150, 92
Bouché N., Murphy M. T., Péroux C., Davies R., Eisenhauer F., Förster Schreiber N. M., Tacconi L., 2007, ApJ, 669, L5
Bregman J. N., Anderson M. E., Miller M. J., Hodges-Kluck E., Dai X., Li J.-T., Li Y., Qu Z., 2018, ApJ, 862, 3
Brook C. B. et al., 2011, MNRAS, 415, 1051
Burgh E. B., France K., McCandliss S. R., 2007, ApJ, 658, 446
Cantalupo S., Arrigoni-Battaia F., Prochaska J. X., Hennawi J. F., Madau P., 2014, Nature, 506, 63
Carlberg R. G., Freedman W. L., 1985, ApJ, 298, 486
Chen H.-W., Kennicutt Robert C. J., Rauch M., 2005, ApJ, 620, 703
Christensen L., Møller P., Fynbo J. P. U., Zafar T., 2014, MNRAS, 445, 225
Corlies L., Peeples M. S., Tumlinson J., O'Shea B. W., Lehner N., Howk J. C., O'Meara J. M., Smith B. D., 2020, ApJ, 896, 125
Courteau S., Dutton A. A., 2015, ApJ, 801, L20
Dutton A. A. et al., 2013, MNRAS, 428, 3183
Dutton A. A., Macciò A. V., 2014, MNRAS, 441, 3359
Epinat B. et al., 2009, A&A, 504, 789
Fixsen D. J., Bennett C. L., Mather J. C., 1999, ApJ, 526, 207
Frank S. et al., 2012, MNRAS, 420, 1731
Fraternali F., 2017, in Fox A., Davé R., eds, Gas Accretion onto Galaxies. Springer, Cham, pp. 323
Freundlich J., Bouché N. F., Contini T., Daddi E., Zabl J., Schroetter I., Boogaard L., Richard J., 2021, MNRAS, 501, 1900
Fynbo J. P. U. et al., 2010, MNRAS, 408, 2128
Genzel R. et al., 2012, ApJ, 746, 69
Genzel R. et al., 2015, ApJ, 800, 20
Genzel R. et al., 2017, Nature, 543, 397
Genzel R. et al., 2020, ApJ, 902, 98
Ginolfi M. et al., 2020, A&A, 633, A90
Guillemin P., Bergeron J., 1997, A&A, 328, 499
Hamanowicz A. et al., 2020, MNRAS, 492, 2347
Husemann B., Bennert V. N., Scharwächter J., Woo J. H., Choudhury O. S., 2016, MNRAS, 455, 1905
Kacprzak G. G., Muzahid S., Churchill C. W., Nielsen N. M., Charlton J. C., 2015, ApJ, 815, 22
Kanekar N. et al., 2018, ApJ, 856, L23
Kanekar N., Prochaska J. X., Neeleman M., Christensen L., Møller P., Zwaan M. A., Fynbo J. P. U., Dessauges-Zavadsky M., 2020, ApJ, 901, L5
Kanekar N., Smette A., Briggs F. H., Chengalur J. N., 2009, ApJ, 705, L40
Klitsch A. et al., 2019a, MNRAS, 482, L65
Klitsch A. et al., 2019b, MNRAS, 490, 1220
Klitsch A., Péroux C., Zwaan M. A., Smail I., Oteo I., Biggs A. D., Popping G., Swinbank A. M., 2018, MNRAS, 475, 492
Klitsch A., et al. 2021, preprint (arXiv:2106.04599)
Kobulnicky H. A., Kennicutt Robert C. J., Pizagno J. L., 1999, ApJ, 514, 544
Kulkarni V. P., Hill J. M., Schneider G., Weymann R. J., Storrie-Lombardi L. J., Rieke M. J., Thompson R. I., Jannuzi B. T., 2000, ApJ, 536, 36
Kulkarni V. P., Hill J. M., Schneider G., Weymann R. J., Storrie-Lombardi L. J., Rieke M. J., Thompson R. I., Jannuzi B. T., 2001, ApJ, 551, 37
Lane W. M., Briggs F. H., Turnshek D. A., Rao S. M., 1998, Bulletin of the American Astronomical Society, 30, 1249
Levy R. C. et al., 2018, ApJ, 860, 92
Loiacono F., Talia M., Fraternali F., Cimatti A., Di Teodoro E. M., Caminha G. B., 2019, MNRAS, 489, 681
Lovell M. R. et al., 2018, MNRAS, 481, 1950
Mangum J. G., Shirley Y. L., 2015, PASP, 127, 266
Martin C. L., Ho S. H., Kacprzak G. G., Churchill C. W., 2019, ApJ, 878, 84
Martin C. L., Shapley A. E., Coil A. L., Kornei K. A., Bundy K., Weiner B. J., Noeske K. G., Schiminovich D., 2012, ApJ, 760, 127
Martinsson T. P. K., Verheijen M. A. W., Westfall K. B., Bershady M. A., Andersen D. R., Swaters R. A., 2013, A&A, 557, A131
McMullin J. P., Waters B., Schiebel D., Young W., Golap K., 2007, in Shaw R. A., Hill F., Bell D. J., eds, ASP Conf. Ser. Vol. 376, Astronomical Data Analysis Software and Systems XVI. Astron. Soc. Pac., San Francisco, p. 127
Mo H. J., White S. D. M., 2002, MNRAS, 336, 112
Molina J. et al., 2020, A&A, 643, A78
Molina J., Ibar E., Smail I., Swinbank A. M., Villard E., Escala A., Sobral D., Hughes T. M., 2019, MNRAS, 487, 4856
Møller P. et al., 2017, MNRAS, 474, 4039
Moster B. P., Naab T., White S. D. M., 2018, MNRAS, 477, 1822
Moster B. P., Somerville R. S., Maulbetsch C., van den Bosch F. C., Macciò A. V., Naab T., Oser L., 2010, ApJ, 710, 903
Muzahid S., Kacprzak G. G., Charlton J. C., Churchill C. W., 2016, ApJ, 823, 66
Muzahid S., Srianand R., Charlton J., 2015, MNRAS, 448, 2840
Navarro J. F., Frenk C. S., White S. D. M., 1997, ApJ, 490, 493
Neeleman M. et al., 2016, ApJ, 820, L39
Neeleman M., Kanekar N., Prochaska J. X., Christensen L., Dessauges-Zavadsky M., Fynbo J. P. U., Møller P., Zwaan M. A., 2018, ApJ, 856, L12
Nelson D. et al., 2020, MNRAS, 498, 2391
Nicastro F. et al., 2018, Nature, 558, 406
Noterdaeme P., Ledoux C., Petitjean P., Srianand R., 2008, A&A, 481, 327
Papadopoulos P. P., van der Werf P., Xilouris E., Isaak K. G., Gao Y., 2012, ApJ, 751, 10
Péroux C. et al., 2016, MNRAS, 457, 903
Péroux C. et al., 2017, MNRAS, 464, 2053
Péroux C. et al., 2019, MNRAS, 485, 1595
Péroux C., Bouché N., Kulkarni V. P., York D. G., Vladilo G., 2011a, MNRAS, 410, 2237
Péroux C., Bouché N., Kulkarni V. P., York D. G., Vladilo G., 2011b, MNRAS, 410, 2251
Péroux C., Nelson D., van de Voort F., Pillepich A., Marinacci F., Vogelsberger M., Hernquist L., 2020, MNRAS, 499, 2462
Pettini M., Pagel B. E. J., 2004, MNRAS, 348, L59
Price S. H. et al., 2020, ApJ, 894, 91
Puech M. et al., 2008, A&A, 484, 173
Rahmani H. et al., 2018a, MNRAS, 474, 254
Rahmani H. et al., 2018b, MNRAS, 480, 5046
Rao S. M., Turnshek D. A., Nestor D. B., 2006, ApJ, 636, 610
Rubin K. H. R., Prochaska J. X., Koo D. C., Phillips A. C., 2012, ApJ, 747, L26
Rudie G. C. et al., 2012, ApJ, 750, 67
Rudie G. C., Newman A. B., Murphy M. T., 2017, ApJ, 843, 98
Saintonge A. et al., 2017, ApJS, 233, 22
Sánchez S. F. et al., 2014, A&A, 563, A49
Sánchez-Menguiano L. et al., 2016, A&A, 587, A70
Schinnerer E. et al., 2019, ApJ, 887, 49
Scoville N. et al., 2017, ApJ, 837, 150
Shen S., Madau P., Aguirre A., Guedes J., Mayer L., Wadsley J., 2012, ApJ, 760, 50
Shull J. M., Danforth C. W., Tilton E. M., 2014, ApJ, 796, 49
Solomon P. M., Downes D., Radford S. J. E., 1992, ApJ, 398, L29

Som D., Kulkarni V. P., Meiring J., York D. G., Péroux C., Lauroesch J. T., Aller M. C., Khare P., 2015, ApJ, 806, 25
Steidel C. C., Erb D. K., Shapley A. E., Pettini M., Reddy N., Bogosavljević M., Rudie G. C., Rakic O., 2010, ApJ, 717, 289
Stewart K. R., Kaufmann T., Bullock J. S., Barton E. J., Maller A. H., Diemand J., Wadsley J., 2011, ApJ, 738, 39
Stinson G. S. et al., 2012, MNRAS, 425, 1270
Suresh J., Rubin K. H. R., Kannan R., Werk J. K., Hernquist L., Vogelsberger M., 2017, MNRAS, 465, 2966
Tacconi L. J. et al., 2018, ApJ, 853, 179
Tremonti C. A. et al., 2004, ApJ, 613, 898
Tripp T. M., Lu L., Savage B. D., 1998, ApJ, 508, 200
Tully R. B., Fisher J. R., 1977, A&A, 500, 105
Tumlinson J., Peeples M. S., Werk J. K., 2017, ARA&A, 55, 389
Turner M. L., Schaye J., Crain R. A., Rudie G., Steidel C. C., Strom A., Theuns T., 2017, MNRAS, 471, 690
Turner M. L., Schaye J., Steidel C. C., Rudie G. C., Strom A. L., 2014, MNRAS, 445, 794
Übler H. et al., 2018, ApJ, 854, L24
Übler H. et al., 2021, MNRAS, 500, 4597
Umehata H. et al., 2019, Science, 366, 97
Weilbacher P. M., Streicher O., Palsa R., 2016, MUSE-DRP: MUSE Data Reduction Pipeline, Astrophysics Source Code Library, record ascl:1610.004
Werk J. K., Prochaska J. X., Thom C., Tumlinson J., Tripp T. M., O'Meara J. M., Peeples M. S., 2013, ApJS, 204, 17
Wisotzki L. et al., 2016, A&A, 587, A98
Wisotzki L. et al., 2018, Nature, 562, 229
Wolfire M. G., Hollenbach D., McKee C. F., 2010, ApJ, 716, 1191
Zabl J. et al., 2019, MNRAS, 485, 1961

APPENDIX A: OBSERVATION DETAILS

We provide further information about the ALMA observations of the MUSE-ALMA haloes sample used in this work and provide additional information about the QSOs and observed galaxies. The additional information can be seen in Table A1.

Table A1. Properties of the quasars and galaxies in the MUSE-ALMA halo sample. Row 1: (1) reference name of the QSO used in this paper, (2) full name of the QSO, (3) right ascension of the QSO, (4) declination of the QSO, (5) QSO redshift, (6) dates for the observations of the field, (7) exposure time of the observation, (8) angular resolution of the observation, (9) calibrators used for the observation, (10) percipitable water vapour (PWV) of the observation, (11) ALMA antenna configuration used for the observation. Row 2: (1) reference name of the galaxy used in this paper, (2) redshifted frequency of the observed CO line, (3) right ascension of the galaxy, (4) declination of the galaxy, (5) redshift of the galaxy, (5) literature references: [a]Hamanowicz et al. (2020).

QSO name	QSO alternative name	RA_{QSO}	DEC_{QSO}	z_{QSO}[a]	Observation dates	T_{exp}	θ	Calibrators	PWV	Ant. config.
Galaxy	f_{CO} [GHz]	RA_{gal} [hh:mm:ss]	DEC_{gal} [dd:mm:ss]	z_{gal}	Detected in CO	[h]	[arc		[mm]	
Q2131−1207	**Q2128−123**	**21:31:35**	**−12:07:04.8**	**0.43**	**4, 5, 7 Jun 2018**	**2.0**	**1.02**	**J2148+0657, J2158−1501**	**0.65–2.8**	**C43-1**
Q2131−G1	241.866	21:31:35.636	−12:07:00.177	0.42974	yes					
Q2131−G2	241.697	21:31:35.775	−12:07:11.558	0.4307[a]	no					
Q1232−0224	**1229−021**	**12:32:00**	**−02:24:04.6**	**1.05**	**26, 28 Jun 2018**	**2.15**	**1.02**	**J1218−0119, J1229+0203**	**1.2–2.2**	**C43-1**
Q1232−G1	247.829	12:31:59.943	−02:24:05.275	0.3953[a]	no					
Q1232−G2	262.462	12:31:59.727	−02:24:12.20	0.7566[a]	no					
Q0152−2001	**UM 675**	**01:52:27**	**−20:01:07.1**	**2.06**	**2, 11, 12 Jul 2018**	**1.5**	**0.96**	**J0006−0623, J0151−1732**	**0.65–2.6**	**C43-1**
Q0152−G1	250.105	01:52:27.827	−20:01:13.991	0.3826[a]	no					
Q1211−1030	**1209+107**	**12:11:41**	**+10:30:02.8**	**2.19**	**23 Aug 2018**	**0.75**	**0.73**	**J1229+0203, J1222+0413**	**0.9–1.2**	**C43-3**
Q1211−G1	248.274	12:11:40.899	10:30:06.990	0.3928[a]	no					
Q1130−1449	**1127−145**	**11:30:07**	**−14:49:27.7**	**1.19**	**4, 8, 15 Dec 2016**	**3.6**	**1.13**	**J1058+0133, J1139−1350**	**1.5–5.4**	**C40-3**
Q1130−G2	263.4	11:30:07.66	−14:49:23.41	0.3127[a]	yes					
Q1130−G4	263.44	11:30:07.62	−14:49:11.44	0.3126[a]	yes					
Q1130−G6	263.67	11:30:08.53	−14:49:28.54	0.3115[a]	yes					

APPENDIX B: Q2131−G1 – KINEMATIC MODELLING RESIDUALS AND MODEL FLUX MAP

The model molecular gas flux map and residuals of the galaxy Q2131−G1 derived from GalPak^{3D} can be seen in Figs B1 and B2. The modelled disc reproduces the observation well, as can be seen by the low residuals.

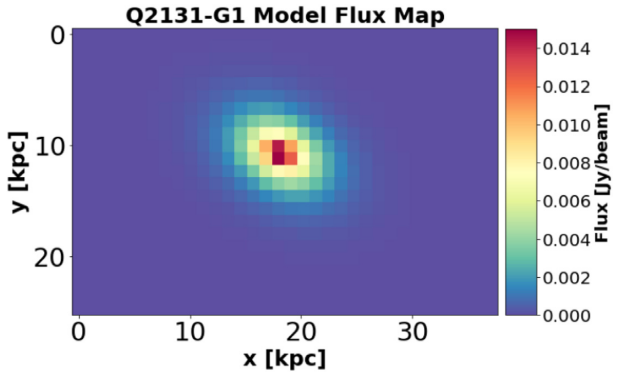

Figure B1. Flux map of Q2131−G1 modelled in 3D-space with GalPak^{3D}.

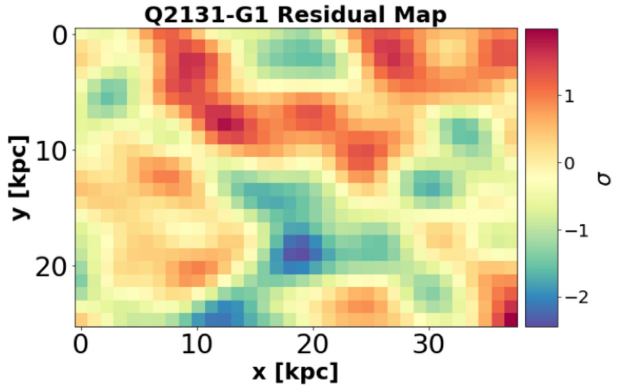

Figure B2. Residual flux map of Q2131−G1 between the modelled and observed fluxes. The low residuals show that the disc model reproduces the observation well. The colour bar displays data – model normalized by the pixel noise σ.

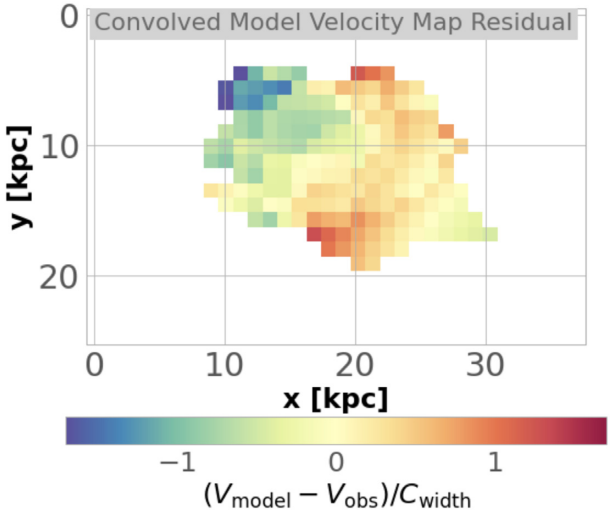

Figure B3. Convolved model velocity map residual. The colour bar is the residual divided by the spectral resolution of the cube ($C_{width} = 50$km s^{-1}). The low residuals across the galaxy indicate that the disc model with an arctan velocity profile reproduces the observations robustly.

This paper has been typeset from a TEX/LATEX file prepared by the author.